

Contents lists available at ScienceDirect

### AdditiveManufacturing

journal homepage: www.elsevier.com/locate/addma



#### Research paper



# Statistical parameterized physics-based machine learning digital shadow models for laser powder bedfusion process

Yangfan Li<sup>a</sup>, Satyajit Mojumder<sup>b</sup>, Ye Lu<sup>a,c</sup>, Abdullah Al Amin<sup>a,d</sup>, Jiachen Guo<sup>b</sup>, Xiaoyu Xie<sup>a</sup>, Wei Chen<sup>a</sup>, Gregory J. Wagner<sup>a</sup>, Jian Cao<sup>a</sup>, Wing Kam Liu<sup>a,1</sup>

<sup>a</sup> Department of Mechanical Engineering, Northwestern University, Evanston, 60208, IL, USA <sup>b</sup> Theoretical and Applied Mechanics Program, Northwestern University, Evanston, 60208, IL, USA <sup>c</sup> Department of Mechanical Engineering, University of Maryland Baltimore County, Baltimore, 21250, MD, USA <sup>d</sup> Department of Mechanical and Aerospace Engineering, University of Dayton, Dayton, 45469, OH, USA

#### ARTICLE

INFO

Keywords:
Physics-based machine learning model
Stochastic calibration
Statistical prediction
Defects diagnostics
Laser powder bed fusion

ABSTRACT

This paper presents a statistical physics-based machine learning model

for predicting defects, such as surface roughness and lack-of-fusion porosity, in the laser powder bed fusion of metals (PBF-LB/M) additive manufacturing process. The statistical physics-based model is calibrated and validated against controlled singletrack experiments and used for statistical prediction for multi-layer and multi-track cases for PBF-LB/M defects. A mechanistic reduced-order-based stochastic calibration process is introduced to capture the stochastic nature of the melt pool. The calibrated physics-based digital shadow model is demonstrated for predicting the surface roughness of the National Institute of Standards and Technology (NIST) overhang part X4, with a difference of 9.3% compared to the experimental results. By leveraging data obtained from both the physics-based model and experiments, a machine learning model has been trained for fast predictions (inference time of 0.4 ms) with high accuracy (error bound of 6.7%). This model can predict melt pool geometries under various processing conditions, offering a control strategy for the PBF-LB/M process. Further, the trained machine learning model is showcased to demonstrate a control application of melt pool geometries (width and depth) for specific processing parameters. These developed models (physics-based and machine learning) serve as a digital shadow of the PBF-LB/M process, offering predictive capabilities to build a digital twin model for process control, optimization, and online monitoring.

#### 1. Introduction

Recent technological advancements, along with the rapid growth in computational power, storage capacity, and data accessibility, have significantly propelled the concept of digital engineering to the forefront within the manufacturing domain [1]. Digital engineering includes the creation of a digital model that integrates physical processes, forming what is known as a digital shadow, and potentially evolving into a digital twin [2,3]. The digital shadow facilitates an automatic, one-way data flow from the physical model to its digital counterpart, thereby enabling real-time updates reflective of changes in the physical world without the capacity for feedback to the physical model. This unilateral data integration is crucial for real-time monitoring and adapting to the changing conditions observed in the physical counterpart. In contrast, a digital twin supports bidirectional, real-time data exchanges between the physical and digital realms. This sophisticated interaction allows

the digital twin not only to receive data but also to send information back to the physical system, thereby enabling control and optimization based on continuous data analysis. Although the digital twin represents the ultimate goal of digital integration, offering extensive control and optimization capabilities, this paper focuses on developing a digital shadow model. We prioritize statistical physics-based predictions and control, serving for future advancement toward a comprehensive digital twin [4].

The Laser Powder Bed Fusion of Metals (PBF-LB/M) additive manufacturing (AM) has achieved significant success and has found extensive applications in the aerospace, automotive, and biomedical industries [5–8], drawing considerable attention in the AM research community. The performance of parts manufactured through PBF-LB/M, such as fatigue, relies on selecting appropriate processing conditions to control structural defects. Defects such as surface roughness and

Received 29 January 2024; Received in revised form 18 April 2024; Accepted 17 May 2024 Available online 19 May 2024

2214-8604/© 2024 Elsevier B.V. All rights are reserved, including those for text and data mining, AI training, and similar technologies.

E-mail address: w-liu@northwestern.edu (W.K. Liu).

<sup>&</sup>lt;sup>1</sup> Corresponding author.

Nomenclature	
α	consolidation factor
β <b>Σ</b>	thermal expansion coefficient (K <sup>-1</sup> ) covariance matrix
η	absorptivity
γ	surface tension (N m <sup>-1</sup> )
	dynamic viscosity (Pa s)
μ	
ρ	material density (kg m <sup>-3</sup> )
$\sigma_s$	Stefan–Boltzmann constant (W m <sup>-2</sup> K-4) emissivity
В	numerical parameter
$C_p$	specific heat (J kg <sup>-1</sup> K <sup>-1</sup> )
D	melt pool depth (m)
d	laser source depth (m)
De	experiment melt pool depth (m)
Ds	simulation melt pool depth (m)
e	linear energy density (J m <sup>-1</sup> )
F	mode function
fı	volume fraction of liquid
${\mathcal G}$	gravitational acceleration (m s <sup>-2</sup> )
Н	hatch spacing (m)
h	bandwidth
i	variable index
j	variable index
K	Gaussian kernel
k	thermal conductivity (W m <sup>-1</sup> K <sup>-1</sup> )
L	layer thickness (m)
M	number of modes
m	mode index
n	number of sample points
NED	normalized energy density
P	laser power (W)
p	pressure (Pa)

$P_1$	calibration parameter					
$P_2$	calibration parameter					
$P_3$	calibration parameter					
PPB - DS	parameterized shadow	physics-based	digital			
PPB - ML - DS	parameterized based learning digit	physics- al shadow	machine			
q <sub>source</sub>	laser heat (W)					
$r_b$	laser source radius (	m)				
RHF	residual heat factor					
Sa	surface roughness (	m)				
$\mathcal{T}$	temperature (K)	temperature (K)				
t	time (s)					
$\mathcal{T}_0$	ambient temperature (K)					
и	velocity (m s <sup>-1</sup> )					
V	scan speed (m s <sup>-1</sup> )					
V ED	volumetric energy d	ensity (J m <sup>-3</sup> )				
W	melt pool width (m)					
We	experiment melt pool width (m)					
Ws	simulation melt pool width (m)					
$x_b$	x coordinates of local reference system (m)					
<i>Yb</i>	y coordinates of local reference system (m)					
Z top	z-coordinate of the top surface (m)					
$T_l$	liquidus melting temperature (K)					
$T_s$	solidus melting tem	perature (K)				

porosity generally originate from suboptimal melt pool formation, often linked to inadequate energy absorption that results in partial melting, or the entrapment of gases due to the vaporization process [9–12]. Understanding the effects of processing conditions on these structural defects is crucial for producing reliable AM parts. A digital shadow of PBF-LB/M process can provide predictions, diagnostic capabilities for defects, and serve as a tool for online monitoring and defects mitigation by controlling the melt pool phenomena. Such a model can also help in comprehending the relationship between the manufacturing process and the resulting part's structure, which is essential for achieving the desired performance in a wide range of applications.

In the PBF-LB/M process, the solid powder undergoes a transformation into liquid state through the application of intense localized heat from a laser. This process inherently carries uncertainty process due to variations in the process parameters, such as laser power, scan speed, fluctuation in boundary temperatures [13–15]. The material parameters (e.g., powder conductivity and absorptivity) are also a major source of uncertainty. As the laser travels through the scan path, the liquid cools and solidifies resulting in the formation of a bulk material with a distinct microstructure. The formation of a melt pool during the laser scan is a crucial aspect that governs the interactions between solid powder materials [16] and influences structural defects such as surface roughness and porosity. The cross-sectional area of the melt pool, typically characterized by its width and depth, indicates the formation of porosity, as inadequate overlap between melt pools can lead to increased porosity [17]. By modeling these uncertain processing conditions, stochastic predictions of the melt pool geometries can provide a more informative estimation of surface roughness and porosity defects.

Previously, deterministic thermal models based on finite element and finite volume methods have been used to model the transient AM process. The predictive accuracy of these models depends on the calibration of the heat source model, the choice of the material properties, and also the fidelity of the geometry and scan path used. For instance, Ghosh et al. [18] developed a finite-volume-based simulation model that effectively captures the melt pool geometries under various laser power and scan speed combinations and validated against experimental data. However, many of these models often overlook the fluid flow within the melt pool, thereby neglecting the impact of cooling through fluid convection, resulting in reduced accuracy in predicting melt pool geometries compared to thermal-fluid flow models that incorporate fluid dynamics, as highlighted by Yan et al. [19]. Notably, Gan et al. introduced a well-tested transient three-dimensional thermalfluid computational model capable of predicting both the thermal field throughout the entire part and the velocity field within the melt pool region [20]. Their model was calibrated using highly controlled experiments conducted during the Additive Manufacturing (AM) Modeling Challenge Series in 2020 [21], ensuring its accuracy

and reliability. However, while this model has demonstrated accurate predictions of melt pool geometries, its limitation lies in the absence of stochastic information which restricts the model's ability to predict surface defects such as surface roughness [22] and volumetric structural defects like porosity [23]. Powder scale simulations have also been considered to simulate surface roughness and porosity for a smaller region in a deterministic manner [24–26]. However, these models are computationally expensive and hinder the inclusion of part scale effects, thereby preventing direct comparisons with experimental measurements conducted at a part scale. Moreover, the deterministic nature of these models further restricts the accuracy of predictions, which require stochastic information and calibration [27–30].

For online monitoring and control of the melt pool, a fast computational model is essential. While physics-based models can provide accurate predictions of the melt pool geometries and defects, the time required for such predictions is often tens of seconds, while rapid predictions (in milliseconds) are needed between printing each layer for control applications. Machine learning (ML) models, leveraging

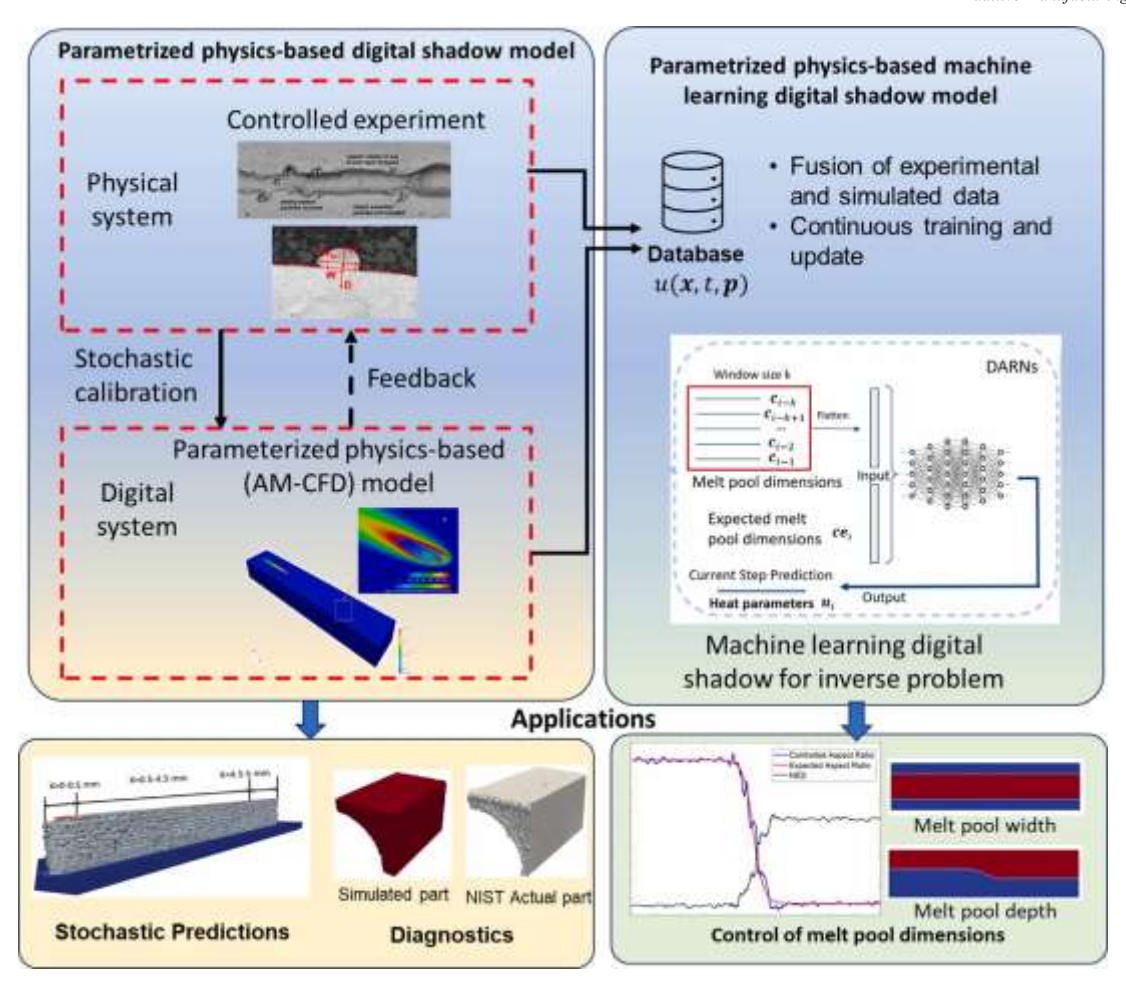


Fig. 1. Physics-based digital shadow model development process and applications.

computational algorithms to analyze and interpret data, can aid on satisfying this fast prediction of melt pool dimensions by learning from an offline database. Liao et al. trained a simulation-guided ML model for the control application in the Directed Energy Deposition (DED) process [31]. Kozjek et al. trained a random forest ML model for the PBF-LB/M process based solely on experimental data [32]. Researchers have also explored Convolutional Neural Networks (CNNs) to effectively and rapidly monitor melt pool dimensions due to their capacity to autonomously and dynamically acquire spatial hierarchies of features [33-35]. The PBF-LB/M AM process is inherently timedependent and embodies a sequential nature. The state of melt pool at any given moment relies on both the current processing parameter inputs and the historical data leading up to that point. Therefore, an ML model that can capture both spatial and the transient behavior of the melt pool following a process history is critical for predicting the process. In this paper, we applied a deep autoregressive network (DARN) for predicting melt pool dimensions [36]. DARNs excel when compared to traditional feed forward neural networks (FFNNs) because they can capture not only the current state of the melt pool, as represented by its width and depth, but also the short-term temporal dependencies within the data that reflect the transient nature of the melt pool. DARNs are specifically designed to handle such temporal dependencies effectively, making them well-suited for predicting and controlling melt pool parameters.

To address the necessity of modeling the stochastic nature of the PBF-LB/M process, this paper introduces a statistical <u>Parameterized Physics-Based Digital Shadow</u> (PPB-DS) model. It accomplishes this through a stochastic calibration of the heat source model parameters, enabling statistical predictions of melt pool geometries and defects such as Lack of Fusion (LOF) porosity and surface roughness. The stochastic calibration of the heat source model of the PBF-LB/M process uses Tensor Decomposition (TD) [37,38], for the learning of non-

intrusive data and construction of reduced-order surrogate models. Experimental data [21], processed from melt pool measurements (see Section 2), is utilized to calibrate the stochastic heat source model parameters and validate it. This PPB-DS model is applied for diagnosing NIST overhang part, especially for LOF porosity and surface roughness. For online monitoring and control applications, a machine learning digital shadow model is trained. This physics-based machine learning digital shadow (PPB-ML-DS) offers predictive capabilities for controlling the processing parameters for subsequent steps of PBF-LB/M tracks.

This paper is organized as follows. In Section 2, we provide an introduction to the two digital shadow models: PPB-DS and PPB-ML-DS, which encompass methodologies of the stochastic calibration process and the DARNs machine learning model. They are used for stochastic prediction, diagnosis of PBF-LB/M defects and control of the melt pool geometries. Section 3 demonstrates the capabilities of the PPB-DS model in statistically predicting melt pool geometries and diagnosing defects such as LOF porosity and surface roughness for part-scale samples. The control applications using the PPB-ML-DS model are also demonstrated in this section. Section 4 provides the discussion of the presented results. Finally, a conclusion and some possible future directions are outlined in Section 5.

#### 2. Digital shadow of laser powder bed fusion process

A digital shadow (DS) model updates its digital representation by continuously receiving data from the physical model, without enabling reciprocal updates. The experimental data can be used for calibrating and validating the physics-based simulation model, and it can also be directly used in conjunction with the simulation data to construct the DS. The calibrated and validated computational model serves as a parameterized physics-based

digital shadow (PPB-DS) model that is capable of predictive and diagnostic applications, as illustrated in Fig. 1. However, certain applications, such as online monitoring and control, demand rapid prediction from the model. The PPB-DS model is not suitable for such predictions, as it requires significant computational time, whereas the responses are needed in real-time. A potential solution for such applications lies in a machine learning-based model trained on the experimental and offline PPB-DS model generated data. Utilizing the database developed through offline PPB-DS computation and experiment, a physics-based machine learning digital shadow model (PPB-ML-DS) is trained to provide rapid prediction of melt pool phenomena.

In this section, we will describe the experimental data available for calibration and validation of our parameterized physics-based stochastic AM model. Then, the methodology for the stochastic calibration process is outlined, that enables the statistical predictions of the melt pool geometries, including the prediction and validation of LOF porosity and surface roughness for part-scale samples. Additionally, we will detail the process of developing the parameterized database and introduce the PPB-ML-DS model along with its training procedure.

### 2.1. Available experimental data for calibration and validation of physicsbased stochastic AM model

Laser powder bed fusion of metals (PBF-LB/M) strongly trigger evaporation with complex gas flow which causes non-uniformity in the printed structure affecting the properties of the printed part. A validated computational model, obtained through a well-designed experiment, is essential for understanding the relationship between process, structure, and properties (PSP) and achieving desired performance in parts. The United States Air Force Research Laboratory: Materials and Manufacturing Directorate Structural Materials, Metals Branch (AFRL/RXCM) and America Make publicly announced the Additive Manufacturing Modeling Challenge Series in 2020. This initiative provided a series of highly controlled additive manufacturing experiments for validation and quantification of computational models [39].

In the AFRL experiment, different cases including single-layer singletrack, single-layer multi-track, and multi-layer single-track (thin-wall) builds of IN625 powder are produced with an EOS M280 commercial PBF-LB/M system. Melt pool dimensions were measured using an electron back-scatter diffraction for top-down track description (Fig. 2a) and optical microscopy on etched cross sections (Fig. 2b). Detailed descriptions of the experimental setup and procedures can be found in the Ref. [21]. To accurately calibrate a stochastic AM model, single-track experiments are utilized to collect statistical measurements. Multi-track and multi-layer cases are then used to validate the melt pool geometry using the single-track calibrated model. Further, surface roughness and lack-of-fusion porosity are measured for the multi-track case and validated against experiments.

To determine the impact of heat source parameters on the melt pool size, it was crucial to analyze how these parameters affected the width ( $\mathcal{W}$ ) and depth ( $\mathcal{D}$ ) of the single-track melt pool. The measured value of the width and depth are shown in Tables 1 and 2, where  $\mu$  represents the mean value and  $\sigma$  denotes the standard deviation. Table 1 demonstrates the different measurements of melt pool width taken at various locations. The fourth column, representing 20 locations, shows the results of measurements conducted by the AFRL AM Modeling Challenge Series. Meanwhile, the fifth to seventh columns, covering 100 to 200 locations, display measurements taken in this study based on the experimental images provided by the AFRL. Similarly, Table 2 compares the melt pool depth between the AFRL measurements and this study. The last column, labeled "Depth", is the sum of the cross-section depth and height.

2.2. Calibrated and validated parameterized physics-based digital shadow (PPB-DS) model

### 2.2.1. Stochastic calibration of the heat source parameters of the physicsbased AM model

A physics-based model of the PBF-LB/M process can capture relevant melt pool phenomena, such as capillary and Marangoni flow, and keyhole formation. While including all melt pool phenomena in a model is theoretically possible, it is computationally prohibitive, making such comprehensive modeling impractical for current applications. Calibration provides an effective way to incorporate these unaccounted-for physics into the model and improve predictions.

However, capturing all the melt pool physics in a model is not feasible and is computationally challenging, and many of these parameters are uncertain. Calibration provides an effective way to account for the unaccounted physics in the model and improve predictions.

Developing a good calibration model requires controlled experiments, and having a large experimental dataset can significantly enhance the model's accuracy in this regard. Predicting surface defects (e.g., surface roughness [40]) and volumetric defects (e.g., porosity [41]) can be improved using a calibrated physics-based model. The accuracy of deterministic simulations in predicting defects, such as surface roughness and porosity, is limited, as it heavily relies on the quality of the model calibration.

To address this issue, we propose a stochastic calibration framework (see Fig. 3) aimed at calibrating the heat source parameters of the physics-based AM model using experimental observations of melt pool geometries. Stochastic AM simulations also allow us to predict surface roughness and porosity in as-built parts, facilitating comparisons with experimental observations.

The stochastic physics-based AM modeling framework consists of the following components: (i) analyzing experimental melt pool geometry (width and depth) to develop a probabilistic model from observations, (ii) creating a thermal-fluid simulation incorporating a statistical heat source model, (iii) calibrating the stochastic heat source model parameters, and (iv) predicting PBF-LB/M process melt pool phenomena and part-scale defects. The melt pool geometries (depth, and width) are obtained by analyzing the controlled AFRL experiment described above (see Section 2.1). Top-down and cross-section of the melt pool images for various processing conditions are analyzed and probability distribution model of the melt pool width (W) and depth (D) is formulated from the experimental observations. The thermal-fluid analysis is based on our in-house code called "AM-CFD". The AM-CFD code has been rigorously tested and confirmed for its accuracy through the 2022 NIST AM Bench challenge, achieving three first-place awards [35,42]. Additionally, its prowess was demonstrated in modeling challenges led by the Air Force Research Laboratory (AFRL), where it secured another first-place award [21,43]. Appendix A provides details about our stochastic physics-based AM-CFD model [20,44].

In our framework as presented in Fig. 3, we introduce stochastic parameters for the heat source model in AM-CFD. These parameters account for the uncertainties caused by variations in real experimental conditions and provide a stochastic prediction of the melt pool geometry. In stochastic calibration process, Kernel density estimation [45] is used to develop a nonparametric distribution of the melt pool geometry. The stochastic AM-CFD predicted melt pool geometry is then statistically compared with the experimental melt pool geometry using Kullback-Leibler divergence (KLD) [46]. The Residual Heat Factor (RHF), as introduced by NIST, has been integrated into our AM-CFD model to better account for variations in scan paths. This integration has demonstrably improved the fidelity of our numerical predictions, enhancing the accuracy of our simulations. For a more comprehensive understanding of the RHF implementation, please refer to Appendix A for a detailed description [44]. To significantly reduce the computational cost for multi-parametric calibration, Tensor Decomposition (TD) is used to handle the AM-CFD heat source model parameters

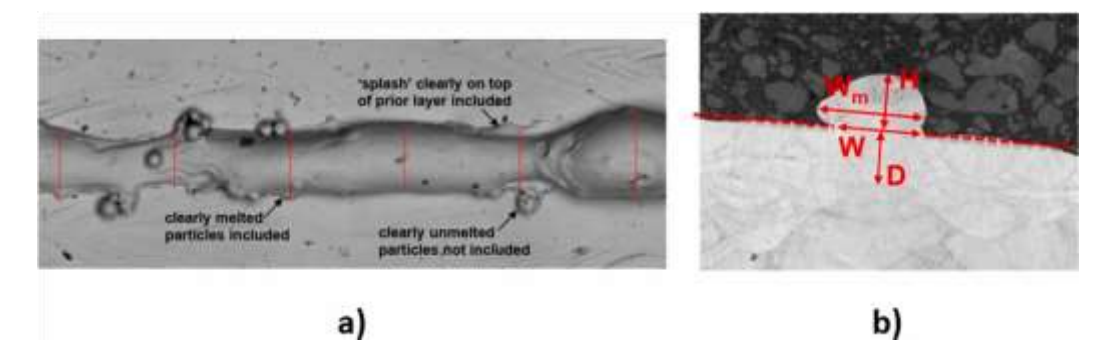


**Fig. 2.** AFRL experiment measurements [39]: (a) Top-down and (b) cross-section melt pool description. In the top-down description, the red lines are samples of melt pool width measurements. In cross-section descriptions, *W* is the width of melt pool, *W*<sub>m</sub> is the largest value of all widths, D and H are the depth and height of the deepest position of melt pool. (For interpretation of the references to color in this figure legend, the reader is referred to the web version of this article.)

Table 1
Width (\(\mu\)m) measurement for 11 single-track cases (A11-A11). AFRL conducted measurements at the 20 locations, while the additional measurements for this study, ranging from 100 to 200 locations, were based on the experimental images provided by AFRL.

Case Number	Laser Power	Scan Speed	20 locations	100 locations	150 locations	200 locations
	(W)	(mm/s)	μ σ	μ σ	μ σ	μ σ
A1	300	1230	112.0 ± 11.1	111.8 ± 11.3	112.0 ± 10.9	111.9 ± 11.0
A2	300	1230	112.0 ± 11.9	111.5 ± 12.5	111.7 ± 12.2	111.8 ± 12.1
A3	290	953	127.6 ± 7.0	125.3 ± 9.4	125.6 ± 10.2	125.5 ± 9.9
A4	370	1230	122.9 ± 8.4	123.2 ± 9.8	122.9 ± 10.2	123.1 ± 10.2
A5	225	1230	96.0 ± 13.9	94.1 ± 13.5	93.1 ± 13.7	93.9 ± 13.3
A6	290	1588	97.9 ± 14.0	94.2 ± 14.3	93.8 ± 13.7	94.1 ± 13.5
A7	241	990	112.0 ± 13.0	110.5 ± 12.4	110.2 ± 11.4	109.8 ± 10.9
A8	349	1430	110.7 ± 11.3	111.8 ± 11.9	111.4 ± 11.3	111.5 ± 11.0
A9	300	1230	112.7 ± 12.7	111.9 ± 11.8	111.8 ± 12.3	112.2 ± 12.2
A10	349	1058	129.9 ± 7.0	127.9 ± 9.3	127.7 ± 9.2	127.7 ± 9.4
A11	241	1529	89.3 ± 12.8	88.6 ± 13.2	88.3 ± 13.5	88.3 ± 13.4

Table 2

Depth measurements (µm) for 11 single-track cases (A1-A11) were conducted in this work and compared with those from the AFRL. Measurements from AFRL and this work are both presented, with the final column representing the 'Depth' as the sum of cross-section depth and height.

Case	Laser	Scan	Cross Section	Cross Section	Cross Section	Cross Section	
Number	Power	Speed	Height (AFRL)	Height (this work)	Depth (AFRL)	Depth (this work)	Sum Depth
	(W)	(mm/s)	$\mu$ $\sigma$	$\mu$ $\sigma$	μ σ	μ σ	$u$ $\sigma$
A1	300	1230	59.1 ± 12.3	59.0 ± 12.9	54.3 ± 9.0	54.3 ± 8.9	113.3 ± 13.4
A2	300	1230	65.7 ± 21.8	65.7 ± 21.7	52.3 ± 9.0	52.5 ± 8.6	118.2 ± 19.9
A3	290	953	68.1 ± 9.2	68.1 ± 9.1	72.0 ± 7.4	72.0 ± 7.4	140.0 ± 12.8
A4	370	1230	66.0 ± 15.5	66.2 ± 15.3	75.9 ± 7.6	75.9 ± 7.2	142.1 ± 17.4
A5	225	1230	60.3 ± 14.9	60.3 ± 14.9	25.0 ± 6.1	25.0 ± 6.1	35.3 ± 13.6
A6	290	1588	62.2 ± 18.3	62.2 ± 18.4	26.9 ± 5.4	27.1 ± 5.6	39.3 ± 19.9
A7	241	990	61.2 ± 11.9	61.2 ± 11.9	42.5 ± 6.6	42.6 ± 7.2	103.8 ± 13.2
A8	349	1430	60.1 ± 15.9	60.1 ± 16.1	58.5 ± 4.6	58.5 ± 4.6	118.5 ± 18.2
A9	300	1230	68.8 ± 25.9	68.8 ± 26.0	46.9 ± 9.3	46.8 ± 8.8	115.5 ± 30.6
A10	349	1058	63.5 ± 17.8	63.3 ± 17.6	84.0 ± 8.9	83.8 ± 8.6	147.1 ± 19.4
A11	241	1529	56.3 ± 18.1	56.3 ± 18.3	20.1 ± 7.1	20.1 ± 7.1	76.4 ± 22.1

calibration problem. The calibrated stochastic AM-CFD can then simulate partscale samples using a Markov chain Monte Carlo (MCMC) method [47] by sampling the calibrated heat source parameters in different time series, with results better than deterministic models. Through this stochastic modeling framework AM-CFD can predict the surface roughness and LOF porosity of the as-built parts by simulating multilayer-multitrack parts.

To calibrate the heat source model, probability density functions (PDF) of experimental melt pool dimensions, width and depth, are calculated using Kernel Density Estimation (KDE) [45]. KDE is a powerful method for estimating the PDF of a random variable. The distributions of the experimental and simulated melt pool width and depth are represented as follows:

$$\frac{-n}{nh}_{j=1} K(\frac{-n}{h})$$

$$f_{W,\delta}(W) = 1 \underbrace{\sum D - D_{\delta j}} (1)$$

$$f_{D,\epsilon}(D) = K(-n)$$

$$\frac{-nh}{nh} h$$

$$\frac{-nh}{nh} (1)$$

$$\frac{-nh}{nh} ($$

nh h this article.)

where  $f_{W e_i} f_{De_i} f_{W s_i} f_{Ds}$  represent distributions of experimental width  $(W_e)$ , experimental depth  $(D_e)$ , simulated width  $(W_s)$  and depth  $(D_s)$ , respectively. K is the Gaussian kernel, f is the index of the sample point, and n is the total number of sample points. Bandwidth is represented as h. Detailed expression can be found in the supplementary document along with a brief overview of KDE. The KDE results are shown in Fig. 4 for the 11 single-track experiment cases in PDF format. These experimental measurements will be used to calibrate the stochastic parameters of the heat source model in AM-CFD in the following section.

Determining the appropriate heat source model parameters is crucial for achieving reliable simulation of the AM process. Multiple

simulations are required to tune these calibration parameters in the model which leads to a significant computational burden. Traditional methods like the genetic algorithm [48] involve repeated calls to the computational model to evaluate the model parameters. To minimize computational expenses, we have integrated a surrogate model named as data-driven tensor decomposition (TD) into our model [37,38]. Datadriven TD is a non-intrusive surrogate model that utilizes a database. The database can be constructed either from simulations or experiments, and the foundation behind TD is the separation of variables technique. This approach accelerates the calibration (identification) process for the heat source model parameters. For a n-dimensional

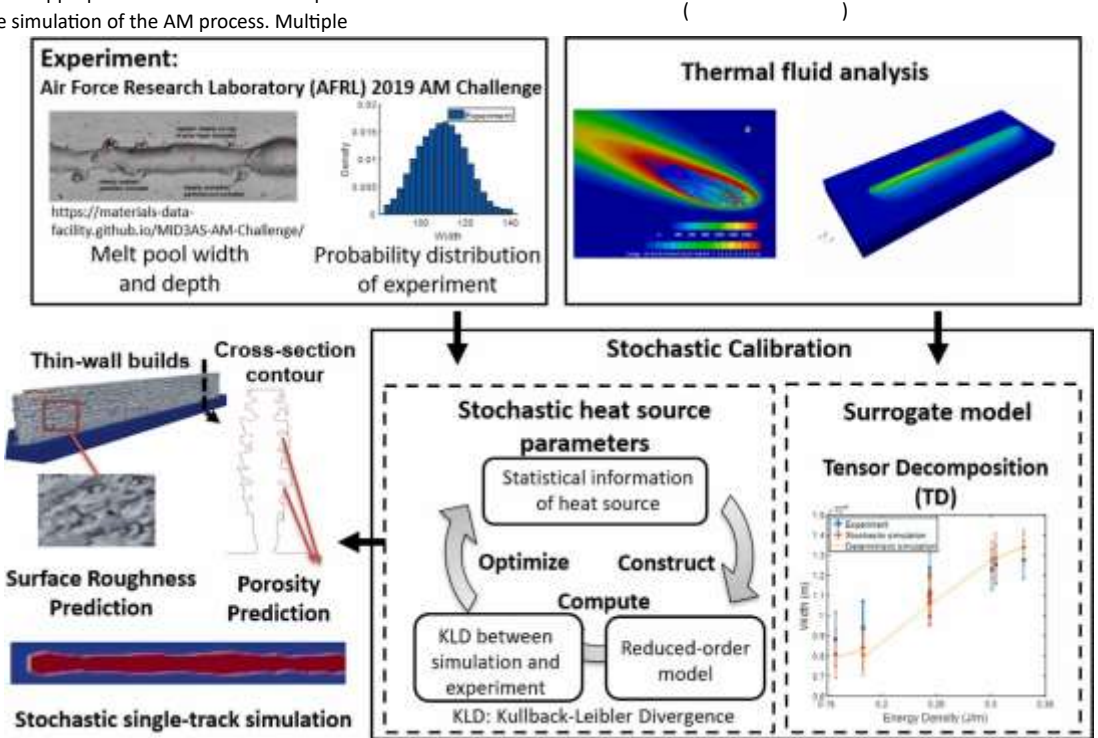


Fig. 3. Stochastic additive manufacturing simulation framework for PBF-LB/M process following a stochastic calibration of the heat source model parameters.

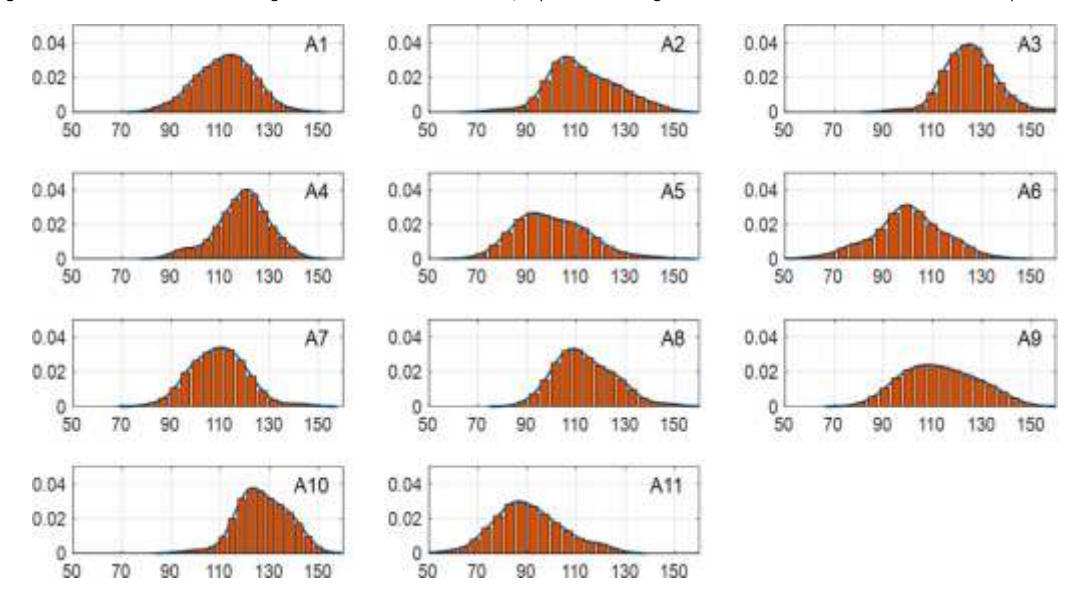


Fig. 4. Experimental measurement (orange bar) and its probability density function generated by KDE (blue line) for melt pool width of single-track experiment case A1 to A11. x-axis represents width (μm), while y-axis is probability density. (For interpretation of the references to color in this figure legend, the reader is referred to the web version of

Y. Li et al. Additive Manufacturing 87 (2024) 104214

function  $f \mu_{1}, \mu_{2}, \mu_{3}, \dots, \mu_{n}$  that contains the quantity of interest as a function of n parameters, TD separation form is given by:

$$f(\mu_1, \mu_2, \mu_3, ..., \mu_n) \approx F_1^{(m)}(\mu_1) F_2^{(m)}(\mu_2) F_3^{(m)}(\mu_3) ..., F_{n(m)}(\mu_n)$$
(5)

The function f is given by the finite sum of products of the separated functions  $F_i^{(m)}(i=1,...,n)$ .  $F_i^{(m)}$  identifies the variation of function f in the parameter direction  $\mu_i$ , which is also called mode function. n is the rank of approximation and m defines the mode number of each component (and not an exponent). M represents the total number of modes. The number of n is a priori unknown and can be obtained with a precomputed physics-based simulation database [49–52]. TD seeks the projection of data for computing the mode functions that can reproduce the original function. This enables TD to serve as a surrogate model for efficient prediction. The surrogate model reduces the computational cost since it only requires 1D interpolation to find output at a given point using the computed mode functions  $F_i^{(m)}$ . The method is suitable for high-dimensional problems due to parse sampling strategy. TD has been applied successfully to accelerate the calibration of welding [50], AM process [53], and microstructural [54] models under deterministic settings.

In this work, the TD method is extended to a stochastic calibration setting. A cylindrical heat source model [12,44,53,55] is used to model the heat input by the laser which is given by:

$$\begin{cases} \left(\begin{array}{ccc} (& (& )) \\ \frac{1}{2P\eta} & \frac{-2 \cdot xz + yz}{b \cdot b} & \leq \\ & & & & & & \\ qsource = \right) & \pi rzbd \exp & rzb & ztop - z & d; \end{cases}$$

$$\begin{cases} \left(\begin{array}{ccc} (& & & & \\ & & & \\ & & & \\ & & & \\ & & & \\ & & & \\ & & & \\ & & & \\ & & & \\ & & & \\ & & & \\ & & & \\ & & & \\ & & & \\ & & & \\ & & & \\ \end{cases}$$

$$\begin{cases} \left(\begin{array}{ccc} (& & & & \\ & & & \\ & & \\ & & \\ & & \\ & & \\ & & \\ & & \\ & & \\ \end{cases}$$

$$Ztop - z \times d \qquad (6)$$

where P denotes the laser power,  $\eta$  is the absorptivity,  $r_{b}$  is the laser beam radius, d is the depth of the heat source, and  $z_{top}$  is the z-coordinate of the top surface of the computational domain.  $x_{b}$  and  $y_{b}$  are the coordinates in the local reference system attached to the moving heat source. Note that the parameters,  $\eta$ ,  $r_{b}$  and d, are all unknown and uncertain heat source parameters, which are highly correlated to the vapor depression phenomenon in the PBF-LB/M process. During calibration, the minimum value of absorptivity is limited to 0.28 [56]. According to the literature [56,57], it has been observed that increasing laser power or decreasing scan speed results in the formation of a vaporinduced depression and increases absorptivity through deepening the keyhole region by multiple reflections of the laser beam between the liquid and gas interface. Therefore, we assume the three parameters,  $\eta$ ,  $r_{b}$  and d are related to the laser power to scan speed ratio P/V, as follows:

$$\frac{P}{V} \qquad d = P_1(7)$$

$$\frac{P}{V} \qquad \eta = \max(P)$$

$$\frac{P}{V} \qquad (0.28)$$
(8)

 $r_b = P_3(9)$ 

 $P_1$ ,  $P_2$ ,  $P_3$  are considered as random parameters and calibrated with the information extracted from melt pool dimension data of AFRL experiments. We assumed that the variation of melt pool reflects the characteristic length of the surface roughness and lack of fusion porosity in the PBF-LB/M process. In this case, the stochastic heat source parameters are assumed to satisfy a tri-variate normal distribution:

$$\begin{pmatrix}
1 & 1 & -\frac{1}{2}(\mathbf{P} - \mathbf{\mu})\tau \mathbf{F} - 1(\mathbf{P} - \mathbf{\mu}) \\
p P_{1}P_{2}P_{3} & = \frac{e}{(2\pi)^{\frac{3}{2}}|\mathbf{F}|^{\frac{3}{2}}}
\end{pmatrix}$$
(10)

where  $\mathbf{P} = [P_1, P_2, P_3]^T$  is the vector of heat parameters,  $\mathbf{\mu} = [\mu 1, \mu 2, \mu 3]^T$   $\begin{bmatrix} c_{11} & c_{12} & c_{13} \end{bmatrix}$  is the mean vector, and  $\mathbf{E} = \begin{bmatrix} c_{21} & c_{22} & c_{23} \end{bmatrix}$  is the covariance  $\begin{bmatrix} c_{23} & c_{33} \end{bmatrix}$ 

matrix. Due to the symmetry of  $\mathcal{L}$ , unknown coefficients are  $\mu_1, \mu_2, \mu_3$ ,  $\mathcal{L}_{11}, \mathcal{L}_{22}, \mathcal{L}_{33}, \mathcal{L}_{12}, \mathcal{L}_{23}, \mathcal{L}_{13}$ . These are the final uncertain hyper-parameters that need to be determined.

In the proposed stochastic AM model, we are trying to capture the process stochasticity through a heat source model, which has proven to be an effective way to account for the dimension and variability of the melt pool in the LPBF process in our previous studies [12,44,55]. We calibrate the heat source parameters to capture the unaccounted physics in the computational model. These parameters: depth of the heat source, absorptivity, and beam radius, are considered significant sources of uncertainty in the LPBF process. The selection of these parameters is based on their substantial impact on the heat distribution within the melt pool, directly affecting energy distribution and material absorption. This, in turn, influences the thermal gradients and solidification rates that are critical for determining the final part quality. Our simulations involve numerous time steps, showing that transient processes statistically converge to a quasi-steady-state distribution. This convergence, where heat source parameters fluctuate within a narrow range, aligns closely with steady-state conditions observed during calibration, thereby supporting the effectiveness of our stochastic model in capturing process variability.

The TD model, which identifies the relationship between the heat source model and key melt pool dimensions (width and depth), is presented below:

$$Y_{s} = F \begin{pmatrix} & & \\ & & \\ & & \\ & & \\ & & \\ e, PF \end{pmatrix} = \sum_{m=1}^{k} F_{1}^{(m)} \left( e \right) \stackrel{(m)}{=} \left( P \right) F_{3}^{(m)} \left( P \right) F_{4}^{(m)} \left( P_{3} \right) \\ & & \\ & & \\ & & \\ & & \\ & & \\ & & \\ & & \\ & & \\ & & \\ & & \\ & & \\ & & \\ \end{pmatrix}$$
(11)

where  $P_1$ ,  $P_2$ ,  $P_3$  are stochastic input heat source model parameters defined in Eq. (10),  $e = V L^P$  is the energy density.  $Y_S$  represents the simulated melt pool dimensions width  $W_S$  or depth  $D_S$ .

Here, the TD model is constructed using a set of sampling data of  $W_s$  and  $D_s$  from deterministic AM simulations for different samples of  $P_1$ ,  $P_2$ ,  $P_3$  in a predefined parameter space. Then, the stochastic output for  $W_s$  and  $D_s$  can be obtained by giving random input of  $P_1$ ,  $P_2$ ,  $P_3$ . It should be noted that an assumption is made here, positing that the width and depth are functions of the heat source at that specific location. This procedure is similar to a surrogate model based MonteCarlo approach for uncertainty propagation. Similar to experimental data, the random output from TD model is estimated using KDE, and denoted by  $f_{W_s}$  and  $f_{D_s}$ .

Using the above TD model, the optimization problem for finding the appropriate hyper-parameters  $p = [\mu_1, \mu_2, \mu_3, C_{11}, C_{22}, C_{33}, C_{12}, C_{23}, C_{13}]$  can be written as

 $P_{\bullet} = arg min / (W_{\bullet}W_{\bullet}P) + / (D_{\bullet}D_{\bullet}P)$  (12) where  $W_{\bullet}$  and  $D_{\bullet}$  are statistical experimental measurements with mean and variance. To define the distance / between experimental and simulated melt pool geometry distributions, the Kullback–Leibler Divergence (KLD) [46] is used. Alternatively, other statistical tests [58] approaches can be considered to determine the discrepancy between the experimental and simulated melt pool geometry distributions. The KLD is a measure of the gap between two distributions, and its lowest value indicates the optimal outcome of probability density estimation. A brief description of the KLD can be found in the supplementary document. The objective function in Eq. (13) can further be defined with KLD:

 $f_{DS(A)}P_1,P_2,P_3$  where  $f_{DS}$  is the index of single-track cases.  $f_{We}$ ,  $f_{De}$ ,  $f_{WS}$ , and  $f_{DS}$  are distributions of experimental width, experimental depth, simulated width and depth that can all be calculated from the KDE method discussed above.

Employing KL divergence is appropriate for assessing how closely the probability distribution of the modeled output (melt pool dimensions) matches the distribution observed in experimental data. KLD divergence focuses on aligning these distributions overall but does not explicitly model the temporal evolution of the process. This is suitable given our current modeling framework, where the primary goal is not focusing on the melt pool shape at a single time step but the overall statistical distribution.

The steps to solve the optimization problem in Eq. (13) are as follows:

- Sample the parameter space with the adaptive sparse grid strategy [50,54] and compute the simulated melt pool dimensions ( W s, Ds) with the AM-CFD model for the selected data points.
- Apply the kernel density estimation (KDE) to the experimental data to obtain the melt pool width and depth distributions

 $f_{We}(W)$  and  $f_{De}(D)$ .

prediction of surface roughness and porosity for part scale simulations at very reduced computation costs while maintaining a high-fidelity computational model. The comparisons between experiment, deterministic simulation (with constant heat source model), and stochastic simulation (with calibrated stochastic heat source model) for the single-track case A1 are illustrated in Fig. 5a. The settings for this experiment were a laser power of 300 W and a scan speed of 1230 mm/s. Fig. 5b compares the distributions of width for the experiment and simulation, which would beneficially demonstrate the minimization of KL divergence and further substantiate the accuracy of our stochastic AM model. The cross-section views in the figure show the variation in the melt pool in stochastic simulations while the deterministic simulations are unable to capture such uncertain information. To assess the accuracy of the stochastic simulations, statistical melt pool geometry, including mean and variance of the width and depth, is compared with experimental observations [39] as shown in Figs. 6 and 7. The figures show energy density for 11 different single-track cases are shown in x-coordinates, while y-coordinates present the melt pool width and depth, respectively. The blue and red error bars represent the mean and variance of the experimental and stochastic simulations, respectively. The yellow line in the figure represents the melt pool dimensions obtained from deterministic simulations. For cases with similar energy density, a zoomed-in view is provided for detailed comparison. To calculate the mean

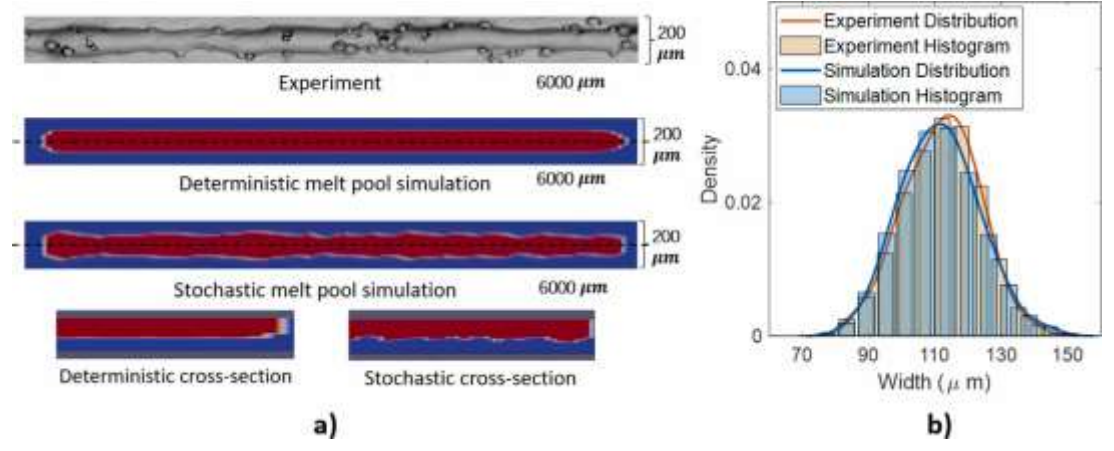


Fig. 5. (a) Comparisons are made between the AFRL experiment [39], deterministic simulation (using a constant heat source model), and stochastic simulation (employing a calibrated stochastic heat source model). The top-down view comparison is shown on the left, while the cross-section view is shown on the right. (b) Comparison of the

- Construct TD surrogate model and compute W s and Ds with Eq. (11) for sample data.
- Generate samples of heat source parameters P<sub>1</sub>, P<sub>2</sub>, P<sub>3</sub>, and obtain stochastic outputs f<sub>WS</sub> and f<sub>DS</sub> based on TD surrogate model.
- Solve the optimization problem in Eq. (13) with KLD method to calibrate the random heat source parameters and find the optimal hyperparameters of the stochastic models.

#### 2.2.2. Validation for single track

distributions for experimental and simulation melt pool widths.

The proposed stochastic AM simulation model provides the capability to predict the variability of the PBF-LB/M melt pool using stochastic process parameters. To predict the stochastic single-track melt pool, we employed the Markov Chain Monte Carlo (MCMC) algorithm [47], which is used for sampling from probability distributions based on time series data. This implies that the sample we consider at any given point is influenced by the preceding samples. Consequently, there is an inherent correlation in the heat source samples across different time steps. MCMC is utilized to generate samples and conduct statistical simulations to predict the relationships between process, structure, and properties.

In each time step of the AM process simulation, MCMC-sampled heat source parameters are imported into AM-CFD program. This approach enables

and variance of melt pool dimensions, 200 locations are measured from both the experimental data and stochastic simulations. The stochastic simulations closely match the experimental melt pool dimensions. In comparison to deterministic simulation, the stochastic simulation captures the uncertainty in melt pool geometry and provides more accurate predictions for most cases.

It is observed that the difference associated with melt width predictions tends to increase at lower energy densities. This increased difference at lower energy densities could be attributed to the model assumptions outlined in Eqs. (A.7) and (A.8) in Appendix A, which do not account for surface tension effects along the z-direction. Including these effects would necessitate a more complex heat source model, significantly increasing computational demands. Our model is designed primarily for large-scale simulation capabilities, balancing the need for computational efficiency with the fidelity of predictions. While this decision has been effective in ensuring the model's applicability across various scenarios, it does introduce some limitations in accurately predicting melt pool width at lower energy densities. However, our model consistently delivers accurate results for melt pool depth across all energy densities. Recognizing the simplifications made, we are considering incorporating z-direction surface tension in future model iterations to enhance accuracy.

## 2.3. Parameterized physics-based machine learning digital shadow model (PPB-ML-DS) model

The choice of a machine learning model over a physics-based simulation model in laser powder bed fusion control is primarily driven by the need for rapid prediction capabilities. In a control setting, where real-time predictions are essential for making rapid adjustments, traditional physics-based simulations can be prohibitively slow and computationally intensive. Machine learning models, on the other hand, can quickly provide predictions by learning patterns and relationships directly from data, allowing for significantly faster inference times. This speed advantage enables actuators to respond promptly to dynamic changes in the melt pool during the additive manufacturing process, ensuring precise control and optimization of parameters in real-time. To develop a rigorous machine learning model, we take advantage of our calibrated and validated PPB-ML-DS model to generate data for continuous training and update.

Among different machine learning tools, we utilize Deep AutoRegressive Networks (DARNs) due to their ability to capture both the current state of the melt pool, including its width and depth, and the short-term temporal dependencies within the data. This capability

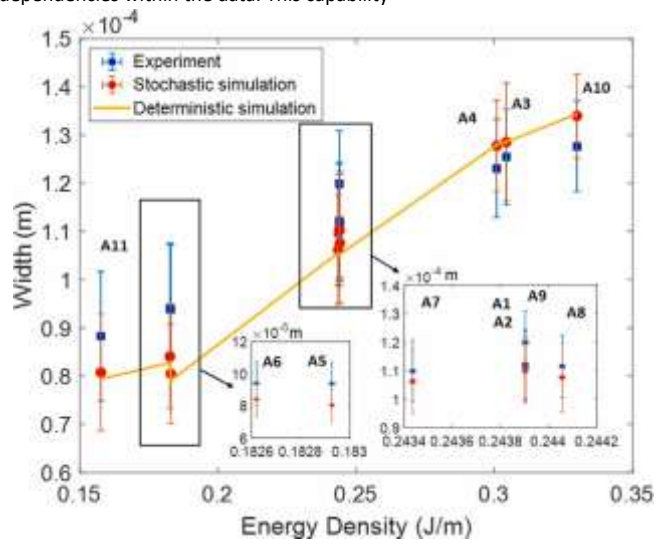


**Fig. 6.** Statistical information of melt pool width between stochastic simulation, deterministic simulation, and experiment. (For interpretation of the references to color in this figure legend, the reader is referred to the web version of this article.)

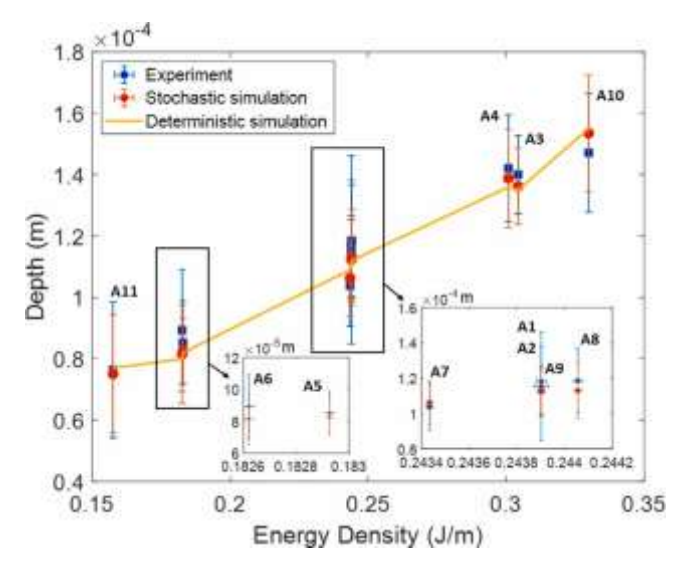


**Fig. 7.** Statistical information of melt pool depth between stochastic simulation, deterministic simulation, and experiment. (For interpretation of the references to color in this figure legend, the reader is referred to the web version of this article.)

makes DARNs particularly suited for predicting and controlling melt pool parameters in laser powder bed fusion, where characteristics often depend not just on present input values but also on recent historical information. By effectively handling these temporal dependencies, DARNs facilitate more accurate and responsive control, optimizing the management of critical heat parameters like normalized energy density, heat source radius, and heat source depth in the additive manufacturing process.

The dimensions of the melt pool, along with the associated heat source parameters, serve as the datasets employed to train and evaluate the DARNs. This dataset encompasses paired observations, where the melt pool's width and depth constitute the input, while the output comprises heat source parameters, specifically normalized energy density (NED), heat source depth, and heat source radius. We utilized twenty-five distinct single-track simulations, each with varying process parameters within the bounds of the AFRL experiment, to generate our datasets. From each simulation, two thousand melt pool dimensions were extracted, resulting in a comprehensive dataset comprising fifty thousand data points. In terms of data distribution, we allocated 70 percent for training, 10 percent for validation, and 20 percent for testing purposes. All datasets were produced using the physics-based AM-CFD solver, the specifics of which are detailed in Appendix A. To ensure the network's effective training, we preprocess the data by applying normalization techniques to standardize the input and output data within a consistent range, thereby preventing issues related to gradient problems during training. NED is a dimensionless number that relates processing parameters and material properties, such as material density, heat capacity, and liquidus temperature. It can be expressed as follows [59]:

$$\eta P = 1 V HL \rho C_v (T_l - T_0)$$

$$NED =$$
 (14)

where  $\eta$  stands for absorptivity,  $\mathcal{P}$  represents laser power,  $\mathcal{V}$  is the scan speed, and  $\mathcal{H}$  denotes the hatch spacing.  $\mathcal{L}$  is the layer thickness,  $\rho$  stands for material density, and  $\mathcal{C}_{\mathcal{P}}$  represents the specific heat. Liquidus and solidus are two temperature denotes the transition of the melting. The solidus melting temperature, denoted as  $\mathcal{T}_{\mathcal{S}_{\mathcal{P}}}$  is the highest temperature at which an alloy is completely solid—where melting begins. The liquidus melting temperature, denoted as  $\mathcal{T}_{\mathcal{N}}$ , is the temperature at which the alloy is completely melted.  $\mathcal{T}_{\mathcal{T}}$  signifies the temperature difference between the liquidus melting temperature and the ambient temperature.

The trained DARNs serve as a PPB-ML-DS model which can solve the inverse problem of process control by controlling the process parameters for melt pool geometry (depth and width). The autoregressive features of DARNs consider the previous 'k' steps as input for each training instance in order to capture the temporal dependencies inherent in melt pool dynamics, where 'k' is defined as the window size. Consider a sequence  $X = (x_0, x_1, x_2, ..., x_T)$  where  $x_T$  denotes the heat source input during AM process (NED, heat source depth and heat source radius). We formulate the model in the following way:

The diagram of the DARN is shown in Fig. 8. Given a window size of k, at time step  $\ell$ , access is limited to historical observations of melt pool dimensions, including melt pool width and depth, represented as  $C_{\ell-1}$ ,  $C_{\ell-2}$ , ...,  $C_{\ell-k}$ , along with the expected width and depth at the current time step, denoted as  $C_{\ell-1}$ . The goal is to establish a function,  $f_{\ell}$ , such that the predicted heat parameters  $\mathbf{u}_{\ell} = f_{\ell}(C_{\ell-1}, C_{\ell-2}, ..., C_{\ell-k}, C_{\ell-k})$ , which provides the most accurate prediction of heat parameter  $\mathbf{u}_{\ell}$  for time step  $\ell$ , aiming to closely match  $\mathbf{x}_{\ell}$  as much as possible.

 $f_A(\cdot)$  can be any parameterized neural network function defined over  $\boldsymbol{\theta}$ . Specifically, we use FFNN in our examples. FFNN is designed to extract features layer-by-layer as defined in the following equations. We utilize h hidden layer FFNN (for our model h = 3) where

$$\mathbf{a}^{(1)} = ReLU(\mathbf{W_0} * \text{input} + \mathbf{B_0})$$
 (15)

 $\boldsymbol{\alpha}(\boldsymbol{I}) = ReLU(\boldsymbol{W}_{I-1} * \boldsymbol{\alpha}(I-1) + \boldsymbol{B}_{I-1})$  (16) output =  $Sigmoid(\boldsymbol{W}_{I-1} * \boldsymbol{\alpha}^{(I-1)} + \boldsymbol{\alpha}^{(I-1)})$ 

 $B_{h-1}$ ) (17)

Note that the learnable parameters in this networks  $\theta = \{W_0, B_0, ..., W_k, B_k\}$ .  $W_k$  and  $B_k$  are the weights and bias of the kth hidden layer.

In order to train  $f_A(\cdot)$ , we utilize maximum likelihood estimation to construct the loss function and solve the following optimization problem:

$$\sum_{i} min_{\boldsymbol{\theta}} \qquad \log {\binom{\mathsf{P}_{xt}(\boldsymbol{u}_{i}|c_{t-1},c_{t-2},...,c_{t-k};c_{t},\boldsymbol{\theta})}{i}}$$
(18)

The conditional distribution of  $\mathcal{U}_{\ell}$  achieve the maximum likelihood when  $\mathcal{U}_{\ell} = \mathcal{X}_{\ell}$ , i.e. the prediction equals the observation results. During the optimization process, the likelihood of  $\mathcal{U}_{\ell}$  increase gradually until the likelihood is maximized over all training data. In practices, we assume  $P_{\mathcal{X}^{\ell}} \sim \mathcal{N}(\mathcal{X}_{\ell}, I)$  follows a Gaussian distribution centered at  $\mathcal{X}_{\ell}$  with identity covariance matrix, therefore, the optimization problem becomes to the following:  $\Sigma_{\ell}$ 

Fig. 8. The DARNs framework is designed to manage the melt pool dimensions. It takes as input the historical dimensions of the melt pool from previous time steps (denoted as  $c_{\ell,1}, c_{\ell,2}, ..., c_{\ell,k+1}, c_{\ell,k}$ ) and the expected dimensions at the current moment ( $ce_{\ell}$ ). The system outputs the forecasted heating parameters ( $u_{\ell}$ ) for the current time step. The objective of DARNs is to derive a function  $f_{\ell}(\cdot)$  that provides a close match between the predicted heat parameters ( $u_{\ell}$ ) and the actual observed values ( $x_{\ell}$ ).

Heat parameters u

The Adam Optimizer is employed for the optimization of the parameter  $\theta$ , as suggested in the work by Kingma and Ba [60]. The network was trained using an initial learning rate of  $1\times 10^{-4}$  across 2450 epochs. Batch training was adopted to providing sufficient update frequency for stable convergence and robust generalization during training, utilizing a batch size of 64.

#### 3. Statistical predictions, defect diagnostics and control application

#### 3.1. Statistical predictions applications of PPB-DS model

Steps

The PPB-DS model is a calibrated and validated physics-based model with stochastic parameterized heat source model. The model is used to simulate multi-layer (thin-wall) and multi-track cases and validate against the AFRL experiment for surface roughness and LOF porosity. A part-scale demonstration of the NIST overhang part is also presented in this section.

#### 3.1.1. Predictions of surface roughness of thin-wall samples

Two thin-wall specimens, B1 and B2, are simulated, each consisting of 10 consecutive layers with a thickness of 40  $\mu m$  and unidirectional scanning track length of 5 mm [39]. All statistical predictions in this section use Inconel 625 alloy. The process parameters for these multilayer specimen are summarized in Table 3. Specimen B1 used a laser power of 300 W and scan speed of 1230 mm/s, and specimen B2 used 241 W and 1529 mm/s. Fig. 9a shows the

simulated result for case B1. For quantitative comparison, the wall is divided into three measurement zones depending on positions (see Fig. 9b). The average height (mean and standard deviation) above the substrate pad datum and the total cross-sectional areas for the entire portion of the wall above the substrate pad datum were measured for each zone as shown in Fig. 9b. Three cross sections are collected within Zones 1 and 3, while approximately 20 cross sections are collected in Zone 2. Fig. 10 presents the comparisons of the three cross sectional area for three different zones between the experimentally measured and computationally predicted values for B1 and B2 multi-track cases. The simulated height and area closely match with the measurements in the second and third zones, indicating the developed model can accurately predict the steady-state melt pool geometry. However, in Zone 1, the beginning region of each layer, the model underestimates the melt pool geometry. This suggests that some transient behaviors occurring at the beginning of each layer are not adequately captured by the model.

Further, the multi-layer case B1 (see Table 3) is simulated using the PPB-DS model to predict the surface roughness and compare with the experiment. Please note that the surface roughness mentioned in this paper specifically refers to the roughness on the sides, which is influenced by the interactions between layers. The laser power for this case was 300 W and scan speed was

1230 mm/s which is a combination of high power and low scanning speed for the Inconel 625 alloy. Fig. 11 presents the PPB-DS predictions of the multi-layer case B1, which manifests the surface roughness due to the stochastic AM process.

The primary roughness parameter reported is the arithmetic mean height (Sa) that evaluates the average standard deviation of the heights from the mean plane (valleys and peaks) in a surface profile to compute the degree of roughness. To compute Sa, first the fitting plane for the points collected from the surface are calculated. Then, the height of a peak or valley is determined by evaluating the height coordinate of each point in the dataset.

The equation of average roughness Sa is given by [61]:

Output

$$Sa = -1 \iint |f(y)| dS \tag{20}$$

A Swhere A is the sampling area and f(y) is height of the profile. The simulated wall is equally divided into 10 regions, and the mean value and variance for the surface roughness is calculated. The calculated surface roughness for case B1 and B2 is  $12.62 \pm 2.61 \, \mu m$ , and  $Sa = 14.57 \pm 3.18 \, \mu m$ , respectively. To understand the effect of processing conditions on surface roughness, we plot the surface roughness against the volumetric energy density (VED) [62], which is defined as:

 $PV\sigma_b t$ 

$$VED = \underline{\hspace{1cm}} \tag{21}$$

where P is laser power, V is scan speed,  $\sigma_{P}$  is the laser beam diameter, and t is the thickness for a single layer. VEDs for B1 and B2 multi-layer cases are 97.56 J/mm³ and 63.05 J/mm³, respectively. The predicted surface roughness for AFRL case B1 and B2, plotted against volumetric energy density, is shown in Fig. 12. This figure compares the simulation results with experimental data on

Inconel 625 [63], with experimental results depicted as dark blue dots. The error bars with red centers represent the statistical variation in the simulated surface roughness. Notably, both experimental and simulation data show relative lower roughness values around a middle VED and have some good alignment, and roughness levels fluctuate within a similar range across the studied VED spectrum. The simulation data also displays larger variance at lower VEDs, offering insights into the impact of energy density on surface roughness.

Table 3

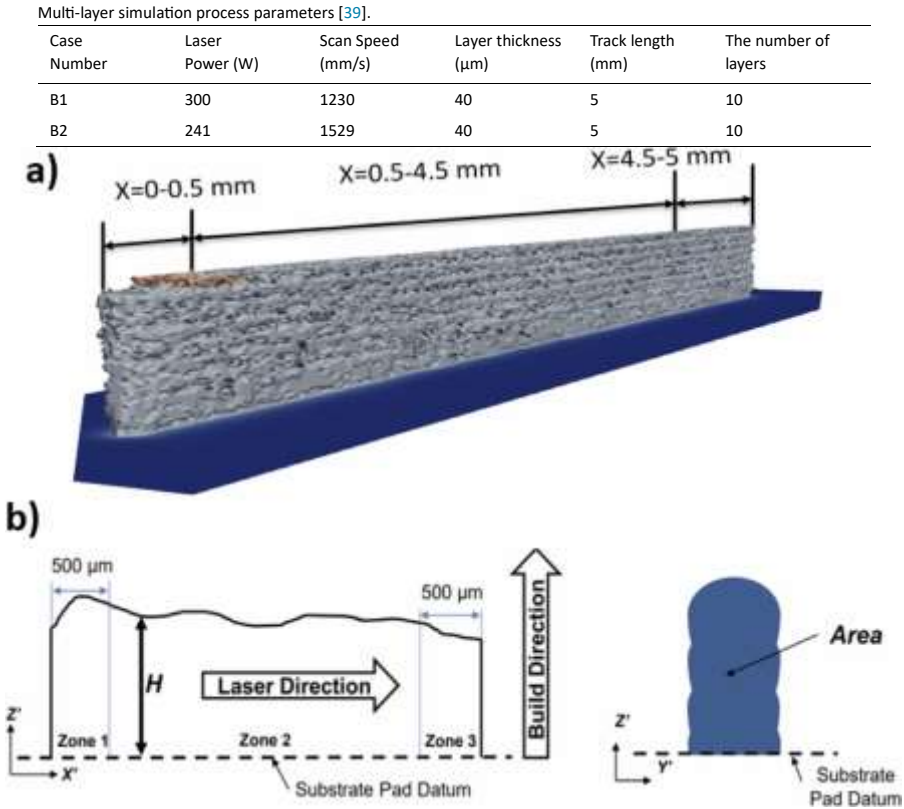
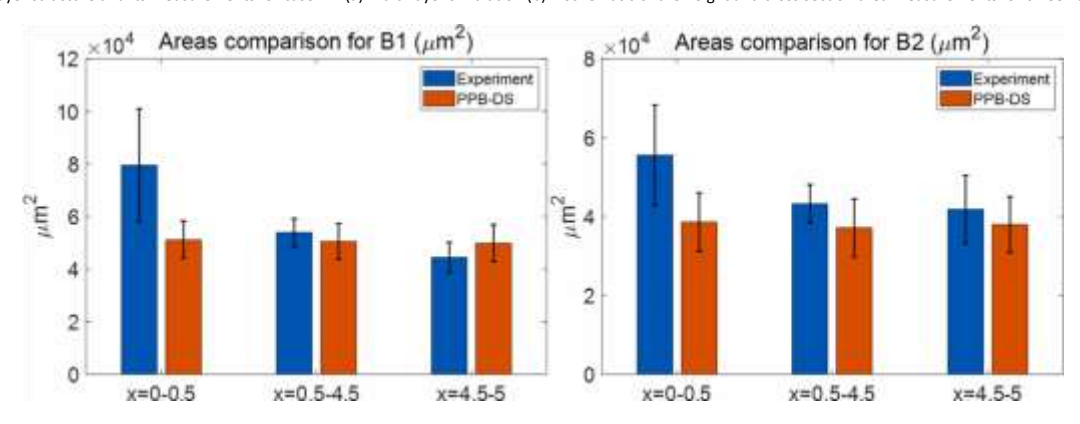


Fig. 9. As-built multi-layer structure and its measurements for case B1. (a) Multi-layer simulation (b) A schematic of the height and cross section area measurements for three Zones [39].



 $\textbf{Fig. 10.} \ \ \textbf{Quantitative comparisons of cross-sectional area between experimental measurements and PPB-DS predictions.}$ 

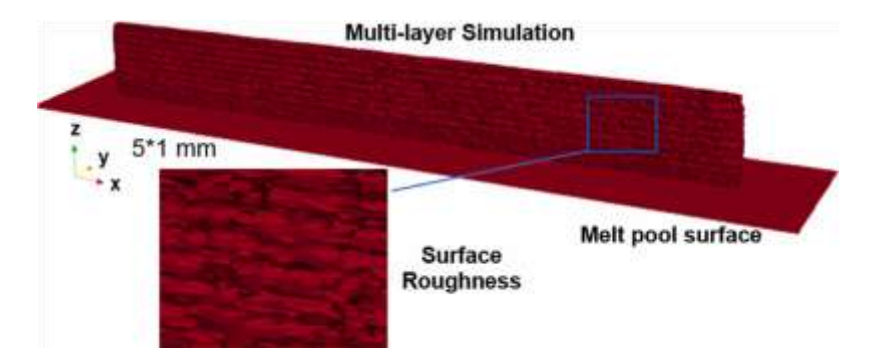
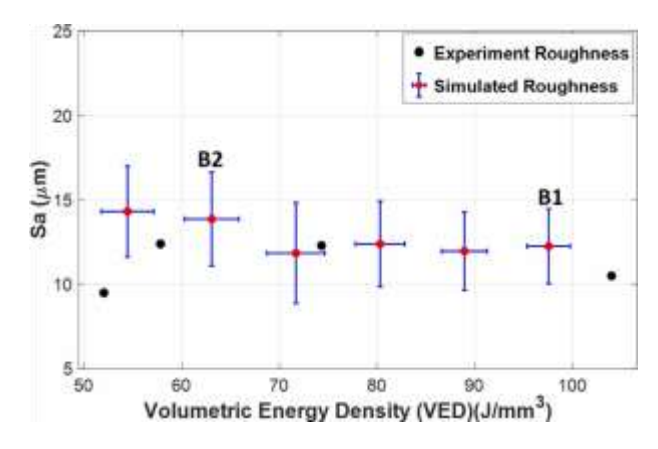


Fig. 11. Surface roughness prediction for multi-layer simulation.

**Table 4**Multi-track simulation process parameters [39].

Case Number	Laser Power (W)	Scan Speed (mm/s)	Hatch Spacing (mm)	Toolpath plane dimensions (mm)	The number of tracks
C1	300	1230	0.1	3*3	30
C2	300	1230	0.1	10*3	30
C3	300	1230	0.075	10*3	40
C4	300	1230	0.125	10*3	24
C5	300	1230	0.1	10*3	30
C6	290	953	0.1	15*3	30



**Fig. 12.** Validation between simulated surface roughness and experimental data [63] under different VEDs (unit: J/mm³). The dark blue dots are experiment measurements. The error bars with a red center illustrate the statistical measurement of simulated surface roughness, in which B1 and B2 have the same VED as the AFRL experiment. (For interpretation of the references to color in this figure legend, the reader is referred to the web version of this article.)

#### 3.1.2. Predictions of melt pool geometries of multi-track samples

Six simulations of multi-track cases were conducted using a calibrated stochastic AM-CFD model to predict the geometrical characteristic of the melted multi-track cases in the PBF-LB/M process. Fig. 13 shows the substrate geometries and tool paths used for these simulations, labeled as C1, C2, C3, C4, C5, C6, corresponding to PBFLB/M experiments performed by AFRL. A dwell time of 0.5 ms was set between the end of scan of one layer to the beginning of the next layer. During this dwell time period, the laser beam was turned off. The black frames show the substrate dimensions, and the arrows represent the laser scan paths. Table 4 summarizes the process parameters used for all six multi-track cases. Fig. 14(a) shows the quantitative comparisons of melted track geometries at the middle of the toolpath (x=1.5 mm) for the six multi-track simulations for the average and standard deviation of the melt pool width (W) and depth (D). The multi-track simulations closely match with experimental data, and demonstrate potential for high-precision AM predictions. Additionally, these simulations can be used for prediction of

surface roughness and LOF porosity at significantly reduced computation costs.

#### 3.1.3. Predictions of LOF porosity for multi-layer and multi-track samples

The PPB-DS model is utilized to predict the surface roughness and LOF porosity for the multi-layer and multi-track cases of AFRL experiments. Additionally, we demonstrate the prediction of surface roughness and LOF porosity for the multi-layer and multi-track cases. Markov chain Monte Carlo sampling is employed to generate timedependent sequences of the processing conditions to simulate the part scale.

For the multi-layer and multi-track cases are investigated for the LOF porosity through our stochastic AM simulation. Fig. 15 shows the multi-layer case B1 (see Table 3) where the porosity is visible in between the layer and near the corner of the track. This porosity occurs due to the improper melting of the powder and tracked in our model by tracking the melting temperature of the scan. Fig. 15 also present the multi-track case, where the LOF porosity is between the consecutive tracks. Also, the multi-track case simulated using stochastic AM model reveals the non-uniform melt pool shape and size distribution which cannot be captured in a deterministic model.

In Fig. 16, the variation of predicted LOF porosity with the volumetric energy density is presented and compared with experimental cases [63]. The LOF porosity decreases as the volumetric energy increases which means a better powder melting scenario. It should be noted that, experimentally measure porosity includes all mode of porosity; however, for the chosen VED ranges, the LOF porosity is the dominant mode and other mechanism of porosity formation is negligible.

#### 3.2. Defect diagnostics for part-scale applications of the PPB-DS model

In this section, a part scale defects diagnostic application is demonstrated using the PPB-DS model. For the demonstration, National Institute of Standards and Technology (NIST) overhang part X4 [64,65] has been used. Same geometry and scan strategy used by NIST for the part has been used in our simulation. However, only 1/8 part of the sample is simulated due to the expensive thermo-fluid simulation in our PPBDS model. The goal of this is to show the defect diagnostic capability of the PPB-DS model for the surface roughness and LOF porosity for a part-scale level.

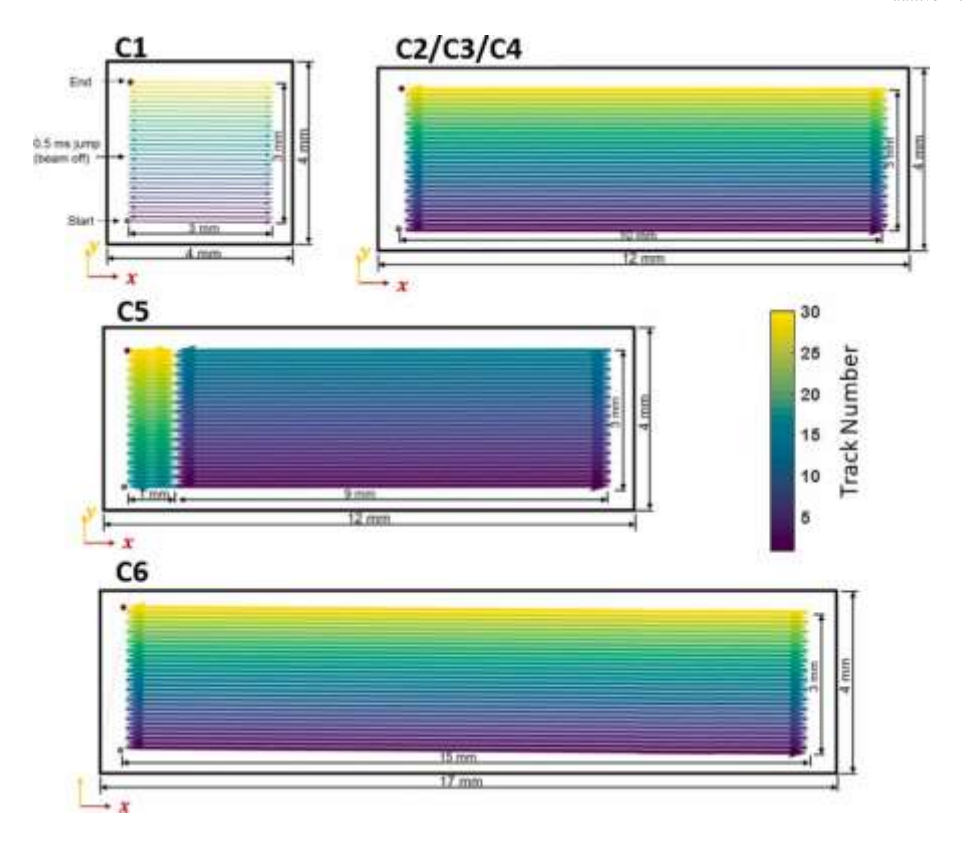


Fig. 13. Scan strategies for the multi-track cases [39]. The start and end points of each track are marked with green and red dots, respectively, and the arrows show the scan paths of the laser, color-coded from violet for the first track to yellow for the last. The colorbar values indicate the track numbers. (For interpretation of the references to color in this figure legend, the reader is referred to the web version of this article.)

**Table 5**Process parameters of NIST overhang part.

P (W)	(mm/s)	Layer Thickness (mm)	Hatch Spacing (mm)	Layer number	Volumetric energy density (J/mm³)
300	800	0.04	0.1	100	101.56

The NIST "Overhang Part X4" [64,65] is fabricated on the Additive Manufacturing Metrology Testbed (AMMT) from nickel superalloy Inconel 625 (IN625). The part has a 9 mm  $\times$  5 mm  $\times$  5 mm rectangular prism shape with a 45° overhang feature and a horizontal cylindrical cutout. Three different view orientations of the computer-aided design (CAD) part geometry is shown in Fig. 17. For demonstration purpose, 1/8 part is simulated and compared with experimental result qualitatively. The dimension of the 1/8 part is 4.5 mm  $\times$  2.5 mm  $\times$  2.5 mm, as demonstrated by the red region in Fig. 17. To enhance the computational speed, we partitioned the entire 100 layers into distinct groups and executed them through a parallel high-performance computing.

The process parameters of the overhang part are shown in Table 5. Fig. 18 presents the surface finish comparison between the NIST experiment and our simulation. Both the experiment and stochastic simulation reveal an irregular and uneven surface when viewed from the front, as well as a rough surface with linear patterns along the top (aligned with the build direction). The proposed stochastic AM simulation is thereby shown to possess the capability of simulating additive manufacturing (AM) parts with defects. The part is divided into five regions to compute the surface roughness of the front surface (as shown in the orange dash lines in Fig. 17). The predicted roughness is  $Sa_{stim} = 13.09 \pm 3.01 \, \mu \text{m}$ , and it has been validated against the experimental roughness measurement  $Sa_{exp} = 14.44 \pm 3.59 \, \mu \text{m}$ , with a difference of 9.3 percent for the mean values. A distribution of the experimental surface roughness is shown with the PPB-DS simulation predicted distribution. Both the distribution matched closely for the mean and the standard deviation (see Fig. 19).

The PPB-DS model can also predict the LOF porosity the NIST part. The predicted LOF porosity is (0.52 $\pm$ 0.24)%. The experimental porosity information is not available for the NIST overhang part.

3.3. Online monitoring and control applications of PPB-ML-ds model

In PBF-LB/M process melt pool monitoring is a crucial aspect to maintain part quality and certification. By controlling the processing parameters such as laser power, speed, etc., desired melt pool geometries can be achieved which can ensure desired performance. However, this is a challenging inverse problem from the modeling perspective where we need to predict the processing conditions for a desired melt pool phenomena. For a control application, such predictions has to be made in real-time (in milliseconds) to control the process for immediate layer. The real-time prediction ability of the machine learning tool motivated us to further develop a machine learning-based digital shadow model for control applications.

In the machine learning model, we set up an inverse problem to predict heat parameters, namely, normalized energy density (NED), heat source radius, and heat source depth for inputs of melt pool width and depth. Specifically, we choose a DARNs model to capture the transient dynamics of the melt pool.

Fig. 20 illustrates the relationship between the number of network epochs and the corresponding loss function of the optimization problem defined in Section 2.3. The loss function quantifies the likelihood across all training data while considering the influence of adjacent data points based on a windowing function. The training and testing data are generated with the physics-based

AM-CFD solver. As depicted in Fig. 20, the training process of our model demonstrates a notable reduction in loss over the course of the epochs. Initially, from epoch 0 to 120, a substantial decrease in loss is observed, followed by a gradual decline in the loss function. Remarkably, the model exhibits ongoing improvement on the evaluation datasets, persisting until epoch 2450.

Furthermore, Fig. 20 provides sub-figures depicting a comparative analysis between the ground truth (represented by the blue line) and the network's predictions (illustrated by the orange line) for the test data sets at various epochs (specifically, epochs 80, 500, and 2450). A clear trend emerges wherein the network's predictions increasingly align with the ground truth as the training progresses. It is worth noting that the *x*-index of the subplots for these comparisons have been sorted by normalized NED in order to clearly represent the results.

Fig. 20 illustrates the discrepancy between the ground truth and network predictions for the test data. The error between the ground truth and prediction is quantified using the following equation. It also demonstrates that the errors remain consistently below 5% for the test data at epoch 2450, employing a window size of 6. This highlights the model's robust performance in accurately predicting the target values, even when considering variations in the input data. The equation for computing the relative error is as follows:

error = 
$$\frac{|X|}{m - Xe|}$$

$$Xe$$
(22)

where  $X_m$  denotes the output from our machine learning model, and  $X_e$  refers to the ground truth data from the experimental measurements.

To assess the control proficiency of our machine learning model, we

prediction time is 0.4 ms, facilitating its real-time control application. Notably,

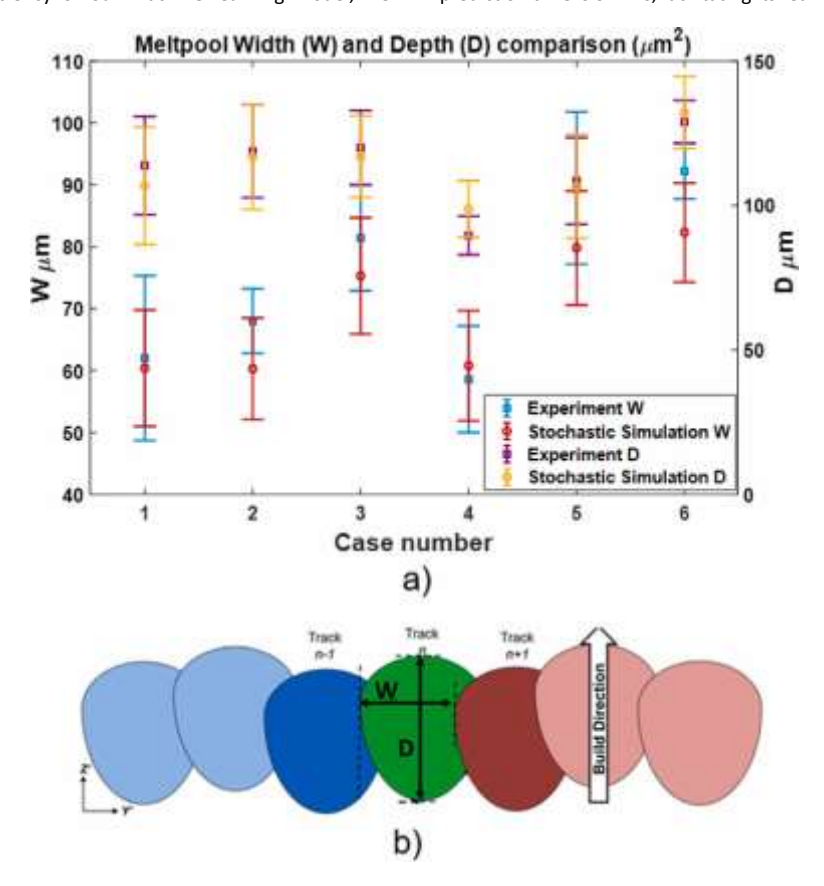


Fig. 14. (a) Quantitative comparisons of melt pool dimensions width (*W*) and depth (*D*) between experimental and stochastic simulations at the middle of the toolpath (x=1.5 mm) for six multi-track cases. The average and standard deviation of each quantity for different tracks are plotted (The error bar represents the standard deviation.) x label "Case number" stands for six multi-track cases. (b) Schematic image of the measurement of melt pool width (W) and depth (D).

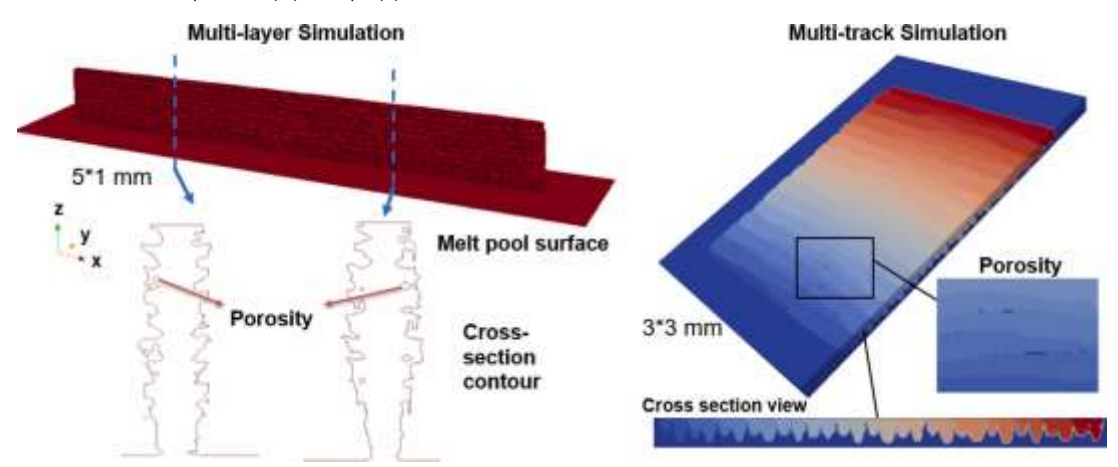


Fig. 15. Porosity prediction for multi-layer and multi-track simulation.

present the desired melt pool depth, which follows the Sigmoid function profile, and we maintain the expected melt pool width at fixed values. The expected aspect ratio of the melt pool, calculated as the width to depth ratio, is represented by the red line in Fig. 21. The corresponding heat source parameters were derived from the PPB-ML-DS model. These parameters were then fed into our physics-based AM-CFD solver to obtain melt pool dimensions. Following that, we derived the aspect ratio from the predicted dimensions, which is depicted by the blue line on the graph, and contrasted with our expected values. The heat source parameters generated by the network, such as NED, are illustrated by the black curve in Fig. 21. The controlled melt pool and width and depth are shown in Fig. 22. The model's

our actual results align closely with the desired melt pool dimensions. The melt pool control is particularly accurate during the steady stages (the initial and final segments of the curve). However, sudden changes in the desired melt pool dimension lead to a slight increase in discrepancies. Most of these deviations remain under 5%, with the largest discrepancy being 6.7%.

#### 4. Discussion

The purpose of using a stochastic model for PPB-DS is to offer a computationally efficient framework that statistically predicts potential defects in the AM process at a specimen scale, such as surface roughness

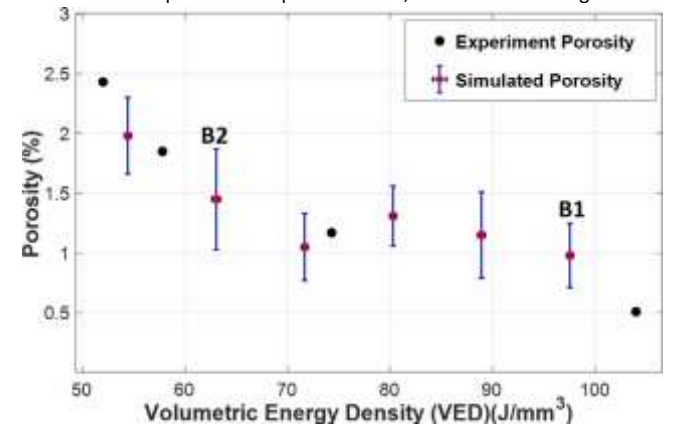


Fig. 16. Validation between simulated porosity and experimental data [63] under different VEDs (unit: J/mm³). The blue dots are experiment measurements. The error bars with red center represent the statistical measurement of simulated porosity, in which B1 and B2 have the same VED as the AFRL experiment. (For interpretation of the references to color in this figure legend, the reader is referred to the web version of this article.)

and porosity. Indeed, the fluctuations of the melt pool observed in the stochastic model might not always capture the real morphological changes due to the simplified physical model and underlying assumptions. Incorporating the time-dependency of melt pool evolution into the calibration could enhance the model's predictive accuracy, which is not considered in the current work. The calibrated hyperparameters are taken as input for our AM-CFD model, and the time dependency of the melt pool is considered as results of the transient CFD analysis only in an implicit manner. Nonetheless, we expect that calibrating hyperparameters using KL divergence will statistically align with the experimentally observed melt pool evolution. The statistical PPB-DS model, therefore, should propagate melt pool variations to other output quantities and enable statistical predictions. Furthermore, this work not focusing on the melt pool shape at a single time step but the overall statistical distribution. The validation test cases confirmed the prediction capability of our methodologies. In our future work, we will further explore the representation of melt pool time dependency in a stochastic model, possibly through a time correction matrix, to further refine the stochastic AM model.

The PPB-DS model, with its stochastic calibration framework, significantly reduces computational effort. In general, multiple-parameter calibration poses a high-dimensional problem that necessitates numerous forward simulations to formulate the optimization problem. Standard approaches such as genetic algorithms [34] have previously been employed for highdimensional calibration problems, requiring the computational model to repeatedly evaluate a trial set of parameters. This results in a computationally expensive model. Conversely, the PPB-DS model constructs a powerful nonintrusive data-driven TD model for the calibration scheme, accelerating the evolution of the trial set of parameters. TD decomposes an n-dimensional problem into a series of one-dimensional problems. It seeks an  $L^2$  projection of data to compute mode functions capable of reproducing or extrapolating the full parametric function. As a result, it serves as a potent surrogate model in the stochastic calibration scheme and significantly reduces the degrees of freedom and computational costs. Having access to more experimental data for calibration can lead to higher prediction accuracy. However, the availability of experimental data is limited, and there is a need for more open data

sources, such as NIST AM Bench, to be contributed by the additive manufacturing (AM) community.

In the current model, uncertainty in the additive manufacturing (AM) process is primarily assumed to stem from the parameters of the heat source model, which are modeled with Gaussian distributions. While the current model demonstrates good predictive performance for melt pool dimensions such as width and depth, it may lack the ability to accurately predict other crucial AM indicators, such as solid cooling rate, liquid cooling rate, and time above melting [55]. To address this limitation, a more intricate stochastic model, such as a Bayesian model, can be employed to characterize the uncertainty of the heat source model. Bayesian models have the advantage of incorporating prior information about the AM process, resulting in more precise estimations.

The proposed methodology has been validated with experimental data from NIST and AFRL across a range of materials including IN625, IN718 [55], Ti-6Al-4V, and SS316L [12], demonstrating its efficacy in predicting melt pool dimensions, cooling rates, times above melting, surface roughness, and LOF porosities. This validation underscores the generalizability of our framework to different manufacturing processes and material systems, provided that stochastic parameters are appropriately tailored based on relevant experimental measurements. Specifically, the stochastic heat source model may remain consistent across alloys if melt pool measurements exhibit similar statistical behaviors. Otherwise, the heat source model should be recalibrated against the measurements for a new material. The model's applicability extends to various geometries without recalibration, as geometric variations do not significantly impact the core physical processes. Similarly, for different toolpaths or build strategies, the existing calibrated parameters generally suffice unless significant deviations in defect characteristics necessitate adjustment. Future refinements may explore deeper integration of materialspecific dynamics to enhance the model's predictive precision and reduce recalibration needs.

The model implicitly accounts for machine variabilities through a stochastic heat source model calibrated against diverse melt pool measurements. While not directly targeting machine variability, the framework facilitates recalibration for different conditions such as gas flow rate, atmosphere, and material systems, ensuring adaptability across various manufacturing settings. With additional experimental data, our model could be able to consider effects like laser switch synchronization and mirror positioning. The flexibility of our stochastic heat source model allows for adaptation without recalibration across different alloys if melt pool data show similar statistical behaviors. Furthermore, the AM-CFD physics model can capture the effects of build orientations and cross-flow by leveraging consistent physical processes, which can be proved by our other project [55]. Variations in build orientation can have a minor impact on defect predictions, such as surface roughness, due to our statistical approach that averages defects across large surfaces. Besides, our model handles changes in melt pool width and depth, demonstrating its ability to integrate crossflow effects. This adaptability underscores the model's potential to provide reliable predictions and reduce the need for recalibrations in diverse manufacturing environments.

The PPB-ML-DS model enables us to make faster predictions for melt pool phenomena. It is important to note that the accuracy of this model depends on several factors, including the choice of machine learning techniques, the quality of the training data, and proper training procedures. In this regard, multi-fidelity data, derived from both experiments and simulations, can be valuable. However, when using experimental data, caution is advised due to the potential presence of noise, which can significantly impact the training process. Using a sophisticated machine learning model may inadvertently focus on fitting the noise rather than accurately representing the underlying physics of the melt pool. In such cases, the PPB-DS model can prove useful, as the data it provides tends to have less noise. However, it may lack certain aspects of the physics if not explicitly considered in the model. To address these challenges and find a balance between different datasets' fidelity while

capturing the essential physics for improved prediction, a transfer learning approach can be a valuable tool.

which significantly reduces the calibration time. We have validated the PPBDS model using AFRL multi-layer and multi-track experiments and demonstrated

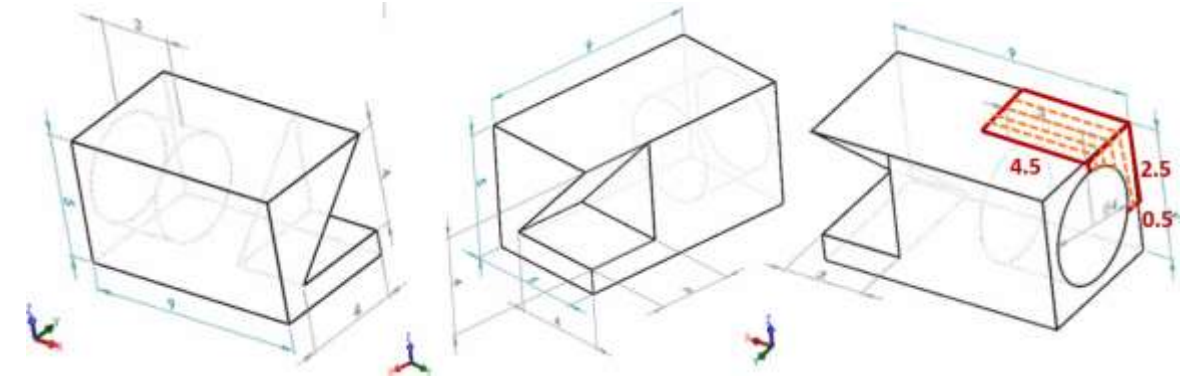


**Fig. 17.** Three view orientations geometry of overhang part (unit:mm), the red region defines the simulation part. (For interpretation of the references to color in this figure legend, the reader is referred to the web version of this article.) its effectiveness in diagnosing defects in NIST overhan

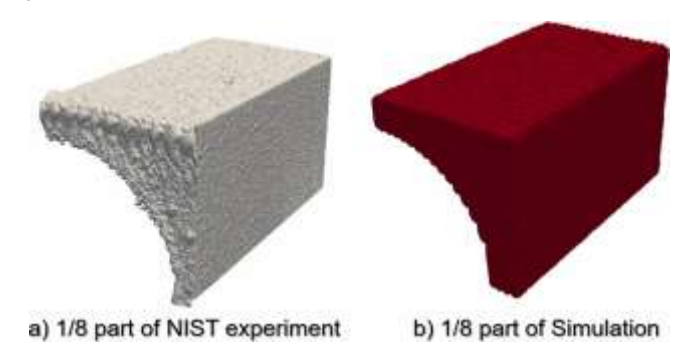


Fig. 18. Comparisons between experimental (a) and simulation (b) result of 1/8 part of Overhang Part X4

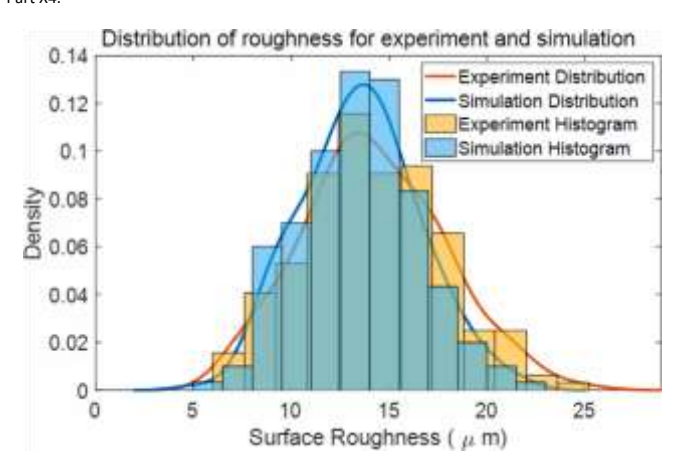


Fig. 19. Comparisons surface roughness distribution and histogram between experimental and simulation for 1/8 part of Overhang Part X4.

#### 5. Conclusions and future directions

In summary, we have developed two digital shadow models, the PPB-DS and PPB-ML-DS, for the laser powder bed fusion of metals. These models have been demonstrated for stochastic melt pool prediction, defect diagnosis, online monitoring, and control applications. The PPB-DS model is a calibrated stochastic physics-based model capable of providing melt pool statistics and offering improved accuracy in predicting surface roughness and LOF porosity. In the stochastic calibration process, we have implemented a mechanistic reduced-order TD model with Markov Chain Monte Carlo (MCMC) sampling,

its effectiveness in diagnosing defects in NIST overhang parts. The PPB-DS model provides statistically predicted surface roughness and porosity for part-scale simulations, aligning closely with experimental distributions, all achieved at a considerably reduced computational cost while maintaining high-fidelity computational modeling. The PPB-ML-DS model is employed for controlling melt pool geometries, allowing real-time process control with rapid prediction capabilities. Ultimately, these modeling and simulation tools enable us to make part-scale predictions of defects and offer insights into control strategies for an effective defect mitigation plan and control strategy for the desired performance of the build parts.

While the current method uses the high-fidelity AM-CFD model to simulate the laser powder bed fusion process, the efficiency of AMCFD is highly constrained by the total number of DoFs (DoFs) in the system. The DoFs increase exponentially as the number of elements in each domain increases. As a result, direct numerical simulation (DNS) of part-scale structures with AM-CFD can be exorbitant. Furthermore, if material parameters, process parameters and boundary conditions are considered as extra-coordinates, the problem will be extremely expensive to solve due to curse of dimensionality. To solve these issues, the statistical space-time-parameter TD solver will be developed in the future as a highly accurate reduced-order method to solve spatial, temporal and parametric domains at the same time. It should be noted here we use TD solver as an intrusive method to directly solve PDEs, which is different from the data-driven TD we previously used in Section 2.2. Thanks to TD, the DoFs grow linearly with respect to the number of elements in each domain. As a result, we expect significant speedup for laser powder bed fusion process simulation.

The current work represents the initial phase of our ongoing effort to develop robust process modeling tools for laser powder bed fusion. In our future endeavors, we plan to expand the stochastic calibration framework to encompass more complex scenarios, including multilayer and multi-track cases with intricate part geometries and tool paths. We have already manufactured a build plate containing 480 samples with varying part shapes, such as cylinders, squares, L-shapes, squares with holes, tapered L-shapes, and overhangs, all of which were closely monitored during the melt pool formation. This extensive dataset will play a crucial role in our future work, enabling us to further enhance the PPB-DS model and train the PPB-ML-DS model for controlling various melt pool parameters, including temperature, depth, width, aspect ratio, and their influence on resulting microstructure. To this aim, a robust process modeling and CA solver are required to be developed.

In the future, we also plan to integrate our proposed stochastic process modeling framework with microstructure modeling tools, such as cellular automation (CA). The proposed stochastic calibration method in this paper only focuses on process modeling. By connecting process modeling with microstructure modeling using CA, we aim to propagate

a) Controlled melt pool width

b) Controlled melt pool depth

#### **CRediT authorship contribution statement**

**Yangfan Li:** Writing – review & editing, Writing – original draft, Visualization, Validation, Software, Methodology, Formal analysis, Data curation, Conceptualization. **Satyajit Mojumder:** Writing – review & editing,

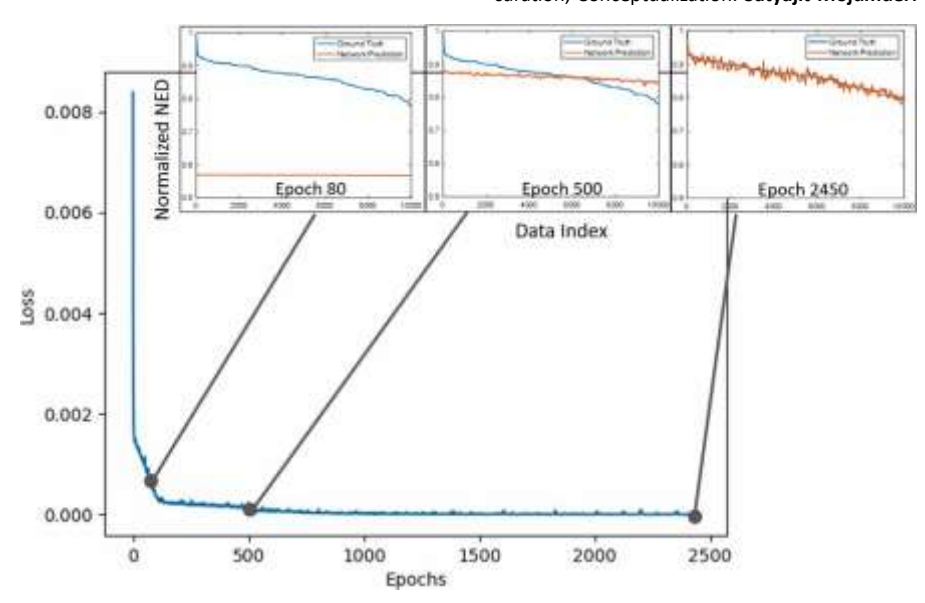


Fig. 20. Loss during the optimization epochs. Each epoch denotes a full iteration over all the training data.

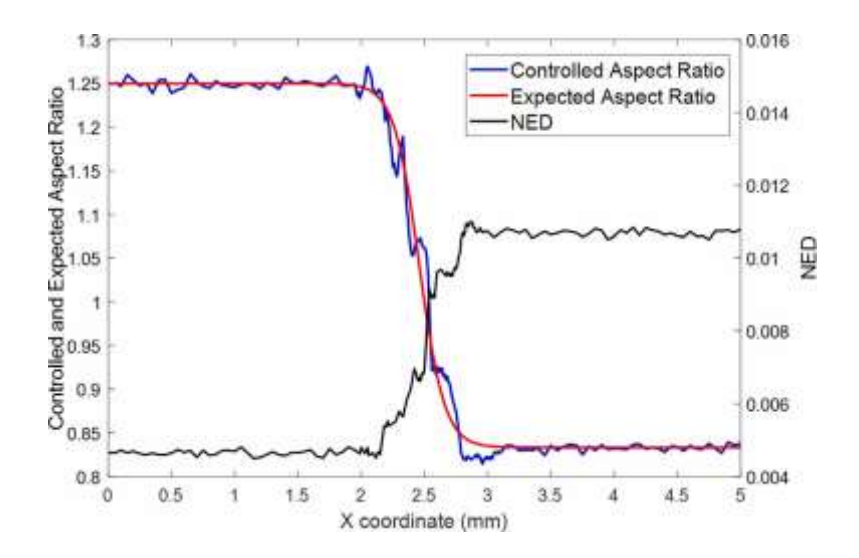


Fig. 21. Comparison of the expected melt pool aspect ratio with the controlled one. The expected aspect ratio are traced by red curves, whereas the blue curves depict the simulations controlled by the heat source parameters produced by the DARNs model. The laser power controlling parameter NED is plotted in black. (For interpretation of the references to color in this figure legend, the reader is referred to the web version of this article.)

Fig. 22. Controlled melt pool (a) width and (b) depth.

the uncertainty from process modeling to microstructure level. Additionally, developing statistical process monitoring and control tools for metallic AM systems is also promising although online monitoring and control still remains to be a major challenge in AM field. For online control purposes, the proposed statistical tool can be further improved in terms of speed for fast online prediction. As a result, when combined with the help of online statistical online monitoring tools from in situ experiments for temperature, porosity, the proposed framework can be extended to an online statistical monitoring and control system.

Writing – original draft, Visualization, Validation, Methodology, Investigation, Conceptualization. Ye Lu: Writing – review & editing, Writing – original draft, Validation, Software, Methodology, Formal analysis. Abdullah Al Amin: Writing – review & editing, Writing – original draft, Visualization, Validation, Software, Methodology, Investigation, Data curation, Formal Analysis, Conceptualization. Jiachen Guo: Writing – review & editing, Visualization, Investigation. Xiaoyu Xie: Writing – review & editing, Data curation. Wei Chen: Writing – review & editing, Visualization, Supervision, Methodology. Gregory J. Wagner: Writing – review & editing, Software, Methodology, Funding acquisition. Jian Cao: Writing – review & editing, Supervision, Software, Methodology. Wing Kam Liu: Writing – review & editing, Supervision, Methodology, Funding acquisition, Conceptualization.

#### **Declaration of competing interest**

The authors declare the following financial interests/personal relationships which may be considered as potential competing interests: Wing Kam Liu reports financial support was provided by National Science Foundation. Jian Cao, Wei Chen reports financial support was provided by National Science Foundation. If there are other authors, they declare that they have no known competing financial interests or personal relationships that could have appeared to influence the work reported in this paper.

#### Data availability

Data will be made available on request.

#### Acknowledgments

W.K. Liu and G.J. Wagner would like to acknowledge the support of The U.S. National Science Foundation (NSF) Grant CMMI-1934367 for up to Section 3 of the paper. W. Chen and J. Cao would like to acknowledge support from the NSF Engineering Research Center for Hybrid Autonomous Manufacturing Moving from Evolution to Revolution (ERC-HAMMER) under Award Number EEC-2133630. Y. Li would like to acknowledge the support of Predictive Science and Engineering Design (PSED) Graduate Program of Northwestern University.

### Appendix A. Thermal-fluid analysis of PBF-LB/M process with stochastic heat source model

To simulate the melted track geometries in the PBF-LB/M process, we perform a thermal-fluid analysis using a stochastic heat source model. This model is an extension of our well-tested AM-CFD code and takes into account the thermal analysis of the entire part while the melt pool region is modeled with fluid dynamics and heat transfer. The governing equations for mass, momentum, and energy conservation were derived to solve the thermal-fluid model [66]:

$$\int_{\Omega f_{I}} (\rho \nabla \cdot \mathbf{u}) dV = 0 \tag{A.1}$$

$$\int_{\Omega f_{I}} (\rho \mathbf{u}) + \nabla \cdot \rho \mathbf{u} \mathbf{u} - \rho \nabla_{2} \mathbf{u} + \nabla \rho$$

$$\int_{\Omega f_{I}} \partial(\rho \mathbf{u}) + \nabla \cdot \rho \mathbf{u} \mathbf{u} - \rho \nabla_{2} \mathbf{u} + \nabla \rho$$

$$\frac{2}{2} + \frac{2}{3 + \beta} \mathbf{u} - \rho \nabla_{2} \beta (T - T_{0}) \mathbf{I} dV = 0$$

$$\int_{C^{2}(f_{I})} (\mathbf{u} \cdot \mathbf{u}) dV = 0$$

$$\int_{\partial (\rho h + \rho \Delta H)} \frac{\partial (\rho h + \rho \Delta H)}{\partial t} + \nabla \cdot (\rho u h + \rho u \Delta H + \nabla \cdot \mathbf{q}) \qquad dV = 0 \quad (A.3)_{\mathcal{Q}}$$

where  $\mathcal{L}$  is the time,  $\mathcal{L}$  is the velocity,  $\mu$  denotes the viscosity,  $\rho$  is the pressure,  $\mathcal{L}$  is the temperature,  $\rho$  is the density, and  $\beta$  is the thermal expansion coefficient.  $\mathcal{L}$  is the acceleration of gravity and equals to 9.8 m/s².  $\rho_0$  and  $\mathcal{L}_0$  are density and temperature of reference material.  $\mathcal{L}$  is the specific enthalpy, and can be divided into the sum of sensible heat  $\hbar$  and the latent heat of fusion  $\mathcal{L}$  In this paper,  $\mu$  is set as a constant,  $\mathcal{L}$  is the approximate primary dendritic spacing, which is set to 1  $\mu$ m.  $\mathcal{L}$  is used to avoid division by zero and set as  $10^{-6}$ 

m.  $\mathcal{Q}f_{I}$  denotes the melt pool region and  $\mathcal{Q}$  is the whole domain.  $f_{I}$  is the volume fraction of the liquid phase, which is defined as:

$$\begin{cases} f_{i}=0 & \text{if} & T \leq T_{s} \end{cases} \begin{cases} f_{i}=TT_{i}-TT_{ss}\text{ if} & T_{s} < T < T_{i}(A.4) \mid f_{i} \end{cases}$$

$$=1 \quad \text{if} \quad T \geq T_{i}$$

where  $\mathcal{T}_s$  and  $\mathcal{T}_l$  are the solidus and liquidus melting temperature of materials, respectively.

Considering  $\bar{\pmb{q}}$  on the surface boundary, heat flex  $\pmb{q}$  and its relation with temperature  $\mathcal{T}$  is

$$\mathbf{q} = -\mathbf{k} \cdot \nabla T \tag{A.5}$$

where k is the thermal conductivity tensor. In isotropic cases, k = kI denotes the second-order identity tensor. The heat source and boundary condition can be written as:

where  $\hbar_{\varepsilon}$  defines the convective heat transfer coefficient,  $\sigma_{s}$  is the Stefan–Boltzmann constant,  $\varepsilon$  is the emissivity,  $\boldsymbol{z}$  is the normal direction of heat source surface.

The heat source  $q_{source}$  from the laser, is described by a cylindrical shape conjugated with Gaussian intensity distribution in AM-CFD program. There are many different heat source models that can be implemented such as cylindrical, semi-spherical, semi-ellipsoidal, conical, radiation heat transfer, ray-tracing, linear decaying, and exponential decaying, which is summarized comprehensively in Ref. [67]. The reason for the choice of cylindrical heat source is due to its ability to appropriately match that of experimental melt pool depth, width, cooling rates, and time above melting. There are also some physical foundations behind such cylindrical heat sources. The depth of the cylindrical heat source is based on the optical penetration depth (OPD). Depending on the powder particle size and distribution, the OPD varies. Usually, the OPD is defined as the depth where the intensity of the laser energy reduces. As the analysis under investigation is on a bare plate, the penetration of energy is assumed uniform along the OPD and related to the total amount of energy that is going into the system. Based on this evidence, the cylindrical heat source is chosen for the problem. The equation of the cylindrical heat source model has been discussed in Section 2

The boundary condition for Eq. (A.2) at the top surface is equal to the main driving force (i.e. Marangoni force):

$$\partial u_x \, d\gamma \, \partial z \qquad dT$$

$$\tau_x = \mu \quad \underline{\hspace{1cm}} = \quad \nabla_x T \qquad (A.7)$$

$$\partial u_y \quad d\gamma$$

$$\tau_y = \mu \quad \underline{\hspace{1cm}} = \quad \underline{\hspace{1cm}} \nabla_y T \qquad (A.8)$$

 $\partial z \ dT$  where  $\gamma$  is the surface tension, which depends on both temperature and materials, and  $d\gamma$  is the temperature coefficient.

The powder layer is treated as a continuous media, and it is distinguished from the substrate through its material properties. A consolidated factor  $\alpha$  ranging from 0 to 1 is used to identify the material state. The value of 0 stands for the material is in the original powder state (no consolidation), while 1

denotes a bulk state (fully consolidated). The definition of  $\alpha$  is:

$$T_{peak} - T_{s}$$

$$\alpha = \frac{}{T_{l} - T_{s}}$$
(A.9)

where  $T_{peak}$  is the local peak energy.

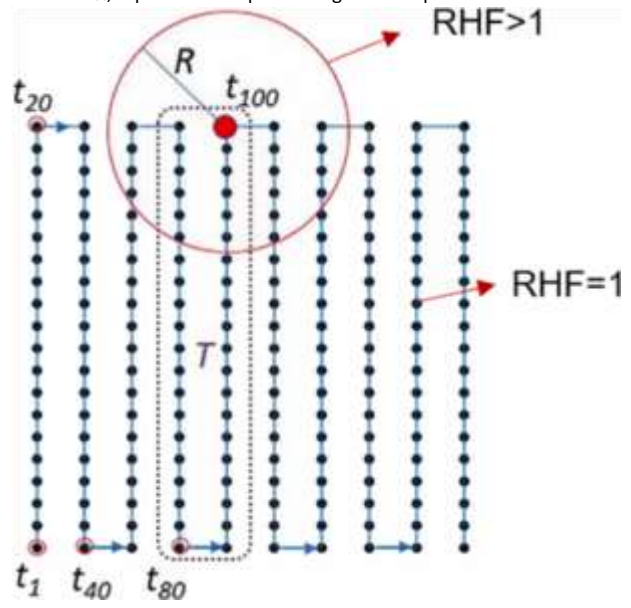
The thermo-physical properties of IN625 are summarized in Table A.6. The densities at ambient and liquidus temperatures are used for solid and liquid densities, respectively. Temperature-dependent polynomials were used for the solid's thermal conductivity and solid's specific heat capacity.

In order to consider the influence of the localized preheating from adjacent scan paths that leads to transient behavior of the vapor depression, the residual heat factor (RHF) is considered into the heat source model [71]. RHF at specific point /is defined as:

$$RHF_{i} = \frac{\sum (R - dik)_{2} (T - tik)}{R} L_{k}$$

$$K \in S_{i}$$
(A.10)

The scan path consists of discrete points determined by the simulation's time step and the laser scan speed. Distance between the point  $\ell$  and  $\ell$ , denoted as  $d_{i\ell_r}$  represents the preheating effect of point  $\ell$  on



point  $\ell$ . Similarly, the elapsed time since point  $\ell$  was scanned is denoted as  $\ell_{\ell \ell}$ . The normalized laser power at point  $\ell$ , denoted as  $\ell_{\ell \ell}$ , is 1 when the laser is on and 0 when laser is off. Constants  $\ell$  and  $\ell$  have values of  $2\times 10^{-4}$  and  $2\times 10^{-3}$ , respectively. These constants act as thresholds to exclude points that have not interacted with the laser for a sufficient amount of time. Points within the threshold belong to set  $\mathcal{S}_{\ell \ell}$  defined as  $\mathcal{S}_{\ell \ell} = \{\ell_{\ell \ell} < T \cup \ell_{\ell \ell} < \ell, \text{ where } \ell > \ell\}$ . The RHF is normalized as  $\ell$  where  $\ell$  where  $\ell$  where  $\ell$  where toolpath and  $\ell$  where toolpath and  $\ell$  where  $\ell$  is greater than 1 at the corner of the toolpath, as shown in Fig. A.23.

Considering the influence of residual heat, the heat source parameters can be coupled with the RHF as:

$$-P$$
(A.11)
$$d = P_1 \quad \text{RHF}$$

$$V$$

$$- P$$

$$(A.12)$$

$$\eta = \max(P_2 \quad \text{RHF}$$

$$V$$

$$\frac{P}{-} r$$

$$b = P_3 V RHF^2$$
(A.13)

The three uncalibrated parameters  $P_1$ ,  $P_2$ ,  $P_3$  necessitate calibration. The methodology for calibrating these parameters is detailed in Section 2.2. **Appendix B. Calibration methods**...

There are multiple ways for optimal estimation of model parameters in probabilistic frameworks. For example, maximum likelihood estimation (MLE),

Table A.6
Thermo-physical properties of IN625 and process constants [39 68–70]

Property/parameter	Value	Property/parameter	Value
Solid density (kg m <sup>-3</sup> )	8440	Convection coefficient (W m <sup>-1</sup> K <sup>-1</sup> )	10
Liquid density (kg m <sup>-3</sup> )	7640	Latent heat of fusion (kJ kg <sup>-1</sup> )	290
Powder density (kg m <sup>-3</sup> )	4330	Dynamic viscosity (Pa s)	7×10 <sup>-3</sup>
Solidus temperature (K)	1563	Thermal expansivity (1/K)	5×10 <sup>-5</sup>
Liquidus temperature (K)	1623	Surface tension (N m <sup>-1</sup> )	1.8
Solid specific heat capacity (J $kg^{-1}K^{-1}$ ) Liquid specific heat capacity (J $kg^{-1}K^{-1}$ )	0.2441 <i>T</i> +338.39 709.25	Marangoni coefficient (N m <sup>-1</sup> K-1) Emissivity	-3.8×10 <sup>-4</sup>
Powder specific heat capacity (J kg <sup>-1</sup> K <sup>-1</sup> )	0.2508 <i>T</i> +357.70	Ambient temperature (K)	295
Solid thermal conductivity (W m <sup>-1</sup> K <sup>-1</sup> )	0.01637 +4.5847	Reference temperature (K)	295
Liquid thermal conductivity (W m <sup>-1</sup> K <sup>-1</sup> )	30.078	Preheat temperature (K)	353
Powder thermal conductivity (W m <sup>-1</sup> K <sup>-1</sup> )	0.995	Stefan–Boltzmann constant (W mm <sup>-2</sup> K <sup>-4</sup> )	5.67×10 <sup>-14</sup>

Fig. A.23. A diagram illustrating a discrete scanning path along with the residual heat factor (RHF) [71].

maximum a-Posteriori (MAP) and Bayesian calibration [72]. Denote the stochastic AM model as  $m(\boldsymbol{p}, \boldsymbol{s})$  where  $\boldsymbol{p}$  is the model parameters,  $\boldsymbol{s}$  can be the

Additive Manufacturing 87 (2024) 104214

initial and boundary conditions. In a calibration processes, we have some observations from experiment and the goal is find the optimal parameters **p**.

In MLE, the optimal parameters are obtained through maximizing? the

likelihood functions :  $p^* = \operatorname{argmax}(p) = \operatorname{argmax} \operatorname{prob} \mathbf{x}_{\ell} | p (B.1)$ 

In MAP, the optimal parameters are obtained through maximizing the posterior probability using the Bayes' rule, where prob(p) is the prior probability of parameters.

prob(
$$|p\rangle$$
) prob( $p\rangle$ )
prob( $p\rangle$ ) =  $|P\rangle$  (B.2)

The optimal parameter can be obtained by maximizing the nominator as:

$$p = \operatorname{argmax}$$
  $\operatorname{prob} \mathbf{x}_{\ell} \mid p \operatorname{prob}(p)$  (B.3)

As can be seen from the equation above, the difference between MLE and MAP is MAP leverages prior probabilities prob(p).

In both MLE and MAP, the calibrated parameter is a constant vector instead of a probability distribution. However, Bayesian calibration can obtain the distribution of the posterior probability of **p** via analyzing the denominator in Eq. (B.2). However, the denominator is generally very expensive to compute if **p** is high dimensional and Monte-Carlo integration is required.

In the proposed approach, the uncertainty of the stochastic AM model originates from the heat source parameters. As shown in Section 2.2, the model parameter p of the stochastic AM simulation is a vector of heat source parameters:  $[\mu_1, \mu_2, \mu_3, C_{11}, C_{22}, C_{33}, C_{12}, C_{23}, C_{13}]$ . As a result, the calibration of our stochastic model aims to find optimal model parameter p such that our stochastic model agrees with observations (evidence) from AFRL experiments. In the proposed approach, the discrepancy f between the experimental and simulated melt pool geometry distributions is defined as the K-L divergence (KLD). The

KLD is a measure of the gap between two distributions, and its lowest value indicates the optimal outcome of probability density estimation. As a result, the optimal parameter p can be obtained by minimizing

• [ ]
$$\mathbf{p}_{=arg\ min} \qquad f(\mathbf{W}_{s}, \mathbf{W}_{e}, \mathbf{P}) + f(\mathbf{D}_{s}, \mathbf{D}_{e}, \mathbf{P})$$
(B.4)

It has been proved minimizing KLD is equivalent to maximizing the likelihood function in Eq. (B.1) [73]. As a result, our calibration method belongs to the family of MLE. The current calibration framework can be extended to MAP and Bayesian by incorporating the prior knowledge of heat source parameters. It should be highlighted that most of current Bayesian calibration methods suffer from curse of dimensionality if the dimension of parameter p is high. This poses challenges for integration in the denominator of Eq. (B.2) since sampling in a high dimensional space can be very expensive. However, since our methods use a separable TD reduced order model, we can easily circumvent curse of dimensionality by using TD.

#### Appendix C. Supplementary data

Supplementary material related to this article can be found online at https://doi.org/10.1016/j.addma.2024.104214.

#### References

- [1] W. Kritzinger, M. Karner, G. Traar, J. Henjes, W. Sihn, Digital twin in manufacturing: A categorical literature review and classification, Ifac-PapersOnline 51 (11) (2018) 1016– 1022
- [2] T. Bergs, S. Gierlings, T. Auerbach, A. Klink, D. Schraknepper, T. Augspurger, The concept of digital twin and digital shadow in manufacturing, Procedia CIRP 101 (2021) 81–84.
- [3] A. Ladj, Z. Wang, O. Meski, F. Belkadi, M. Ritou, C. Da Cunha, A knowledgebased Digital Shadow for machining industry in a Digital Twin perspective, J. Manuf. Syst. 58 (2021) 168–179
- [4] M. Sjarov, T. Lechler, J. Fuchs, M. Brossog, A. Selmaier, F. Faltus, T. Donhauser, J. Franke, The digital twin concept in industry—a review and systematization, in: 2020 25th IEEE International Conference on Emerging Technologies and Factory Automation, Vol. 1, ETFA, IEEE, 2020, pp. 1789–1796.
- [5] V. Petrovic, J.V.H. Gonzalez, O.J. Ferrando, J.D. Gordillo, J.R.B. Puchades, L.P. Griñan, Additive layered manufacturing: sectors of industrial application shown through case studies, Int. J. Prod. Res. 49 (4) (2011) 1061–1079.
- [6] C. Yan, L. Hao, A. Hussein, D. Raymont, Evaluations of cellular lattice structures manufactured using selective laser melting, Int. J. Mach. Tools Manuf. 62 (2012) 32–38.
- [7] N. Guo, M.C. Leu, Additive manufacturing: technology, applications and research needs, Front Mech Eng 8 (3) (2013) 215–243.
- [8] Standard for Laser Beam Powder Bed Fusion of Metals, ASTM International, Conshohocken, PA, 2022.
- [9] R. Cunningham, S.P. Narra, C. Montgomery, J. Beuth, A. Rollett, Synchrotronbased X-ray microtomography characterization of the effect of processing variables on porosity formation in laser power-bed additive manufacturing of Ti-6Al-4V, Jom 69 (3) (2017) 479– 484.
- [10] M. Tang, P.C. Pistorius, J.L. Beuth, Prediction of lack-of-fusion porosity for powder bed fusion, Addit. Manuf. 14 (2017) 39–48.
- [11] A. Yadollahi, N. Shamsaei, Additive manufacturing of fatigue resistant materials: Challenges and opportunities, Int. J. Fatigue 98 (2017) 14–31.
- [12] S. Mojumder, Z. Gan, Y. Li, A. Al Amin, W.K. Liu, Linking process parameters with lack-offusion porosity for laser powder bed fusion metal additive manufacturing, Addit. Manuf. 68 (2023) 103500.
- [13] Z. Hu, S. Mahadevan, Uncertainty quantification and management in additive manufacturing: current status, needs, and opportunities, Int. J. Adv. Manuf. Technol. 93 (5) (2017) 2855–2874.
- [14] Y. Li, Y. Wang, R. Ma, P. Hao, Improved reliability-based design optimization of non-uniformly stiffened spherical dome, Struct. Multidiscip. Optim. 60 (1) (2019) 375–392.
- [15] T. Moges, G. Ameta, P. Witherell, A review of model inaccuracy and parameter uncertainty in laser powder bed fusion models and simulations, J. Manuf. Sci. Eng. 141 (4) (2019).
- [16] P. Witherell, S. Feng, T.W. Simpson, D.B. Saint John, P. Michaleris, Z.-K. Liu, L.-Q. Chen, R. Martukanitz, Toward metamodels for composable and reusable additive manufacturing process models, J. Manuf. Sci. Eng. 136 (6) (2014).
- [17] C. Qiu, Z. Wang, A.S. Aladawi, M.A. Kindi, I.A. Hatmi, H. Chen, L. Chen, Influence of laser processing strategy and remelting on surface structure and porosity development during selective laser melting of a metallic material, Metall. Mater. Trans. A 50 (9) (2019) 4423– 4424.
- [18] S. Ghosh, L. Ma, L.E. Levine, R.E. Ricker, M.R. Stoudt, J.C. Heigel, J.E. Guyer, Single-track melt-pool measurements and microstructures in Inconel 625, Jom 70 (6) (2018) 1011– 1016.
- [19] W. Yan, Y. Lu, K. Jones, Z. Yang, J. Fox, P. Witherell, G. Wagner, W.K. Liu, Data-driven characterization of thermal models for powder-bed-fusion additive manufacturing, Addit. Manuf. 36 (2020) 101503.
- [20] Z. Gan, K. Jones, Y. Lu, W. Liu, Benchmark study of melted track geometries in laser powder bed fusion of Inconel 625, Integr. Mater. Manuf. Innov. 10 (2) (2021) 177–195.
- [21] E.J. Schwalbach, M.G. Chapman, M.A. Groeber, AFRL additive manufacturing modeling series: Challenge 2, microscale process-to-structure data description, Integr. Mater. Manuf. Innov. 10 (3) (2021) 319–337.
- [22] J. Zhao, M. Easton, M. Qian, M. Leary, M. Brandt, Effect of building direction on porosity and fatigue life of selective laser melted AlSi12Mg alloy, Mater. Sci. Eng. A 729 (2018) 76–
- [23] H. Zhang, M. Xu, Z. Liu, C. Li, P. Kumar, Z. Liu, Y. Zhang, Microstructure, surface quality, residual stress, fatigue behavior and damage mechanisms of selective laser melted 304L stainless steel considering building direction, Addit. Manuf. 46 (2021) 102147.
- [24] G. Strano, L. Hao, R.M. Everson, K.E. Evans, Surface roughness analysis, modelling and prediction in selective laser melting, J. Mater. Process. Technol. 213 (4) (2013) 589–597.
- [25] D. Wu, Y. Wei, J. Terpenny, Surface roughness prediction in additive manufacturing using machine learning, in: International Manufacturing Science and Engineering Conference, in: Manufacturing Equipment and Systems, Vol. 3, 2018.
- [26] J. Ning, D.E. Sievers, H. Garmestani, S.Y. Liang, Analytical modeling of part porosity in metal additive manufacturing, Int. J. Mech. Sci. 172 (2020) 105428.
- [27] W. Zhang, R. Bostanabad, B. Liang, X. Su, D. Zeng, M.A. Bessa, Y. Wang, W. Chen, J. Cao, A numerical Bayesian-calibrated characterization method for multiscale prepreg

- preforming simulations with tension-shear coupling, Compos. Sci. Technol. 170 (2019) 15–24.
- [28] W. Li, S. Chen, Z. Jiang, D.W. Apley, Z. Lu, W. Chen, Integrating bayesian calibration, bias correction, and machine learning for the 2014 sandia verification and validation challenge problem. J. Verif. Valid. Uncertain. Quant. 1 (1) (2016) 011004.
- [29] P.D. Arendt, D.W. Apley, W. Chen, Quantification of model uncertainty: Calibration, model discrepancy, and identifiability, 2012.
- [30] P.D. Arendt, D.W. Apley, W. Chen, D. Lamb, D. Gorsich, Improving identifiability in model calibration using multiple responses. 2012.
- [31] S. Liao, S. Webster, D. Huang, R. Council, K. Ehmann, J. Cao, Simulation-guided variable laser power design for melt pool depth control in directed energy deposition, Addit. Manuf. 56 (2022) 102912.
- [32] D. Kozjek, F.M. Carter III, C. Porter, J.-E. Mogonye, K. Ehmann, J. Cao, Datadriven prediction of next-layer melt pool temperatures in laser powder bed fusion based on co-axial highresolution Planck thermometry measurements, J. Manuf. Process. 79 (2022) 81–90.
- [33] B. Yuan, G.M. Guss, A.C. Wilson, S.P. Hau-Riege, P.J. DePond, S. McMains, M.J. Matthews, B. Giera, Machine-learning-based monitoring of laser powder bed fusion, Adv. Mater. Technol. 3 (12) (2018) 1800136.
- [34] X. Li, X. Jia, Q. Yang, J. Lee, Quality analysis in metal additive manufacturing with deep learning, J. Intell. Manuf. 31 (2020) 2003–2017.
- [35] Z. Yang, Y. Lu, H. Yeung, S. Krishnamurty, Investigation of deep learning for real-time melt pool classification in additive manufacturing, in: 2019 IEEE 15th International Conference on Automation Science and Engineering, CASE, IEEE, 2019, pp. 640–647.
- [36] K. Gregor, I. Danihelka, A. Mnih, C. Blundell, D. Wierstra, Deep autoregressive networks, in: International Conference on Machine Learning, PMLR, 2014, pp. 1242–1250.
- [37] Y. Lu, H. Li, L. Zhang, C. Park, S. Mojumder, S. Knapik, Z. Sang, S. Tang, D.W. Apley, G.J. Wagner, et al., Convolution Hierarchical Deep-learning Neural Networks (C-HiDeNN): finite elements, isogeometric analysis, tensor decomposition, and beyond, Comput. Mech. (2023) 1–30.
- [38] H. Li, S. Knapik, Y. Li, C. Park, J. Guo, S. Mojumder, Y. Lu, W. Chen, D.W. Apley, W.K. Liu, Convolution Hierarchical Deep-Learning Neural Network Tensor Decomposition (C-HiDeNN-TD) for high-resolution topology optimization, Comput. Mech. (2023) 1–20.
- [39] M.E. Cox, E.J. Schwalbach, B.J. Blaiszik, M.A. Groeber, AFRL additive manufacturing modeling challenge series: Overview, Integr. Mater. Manuf. Innov. 10 (2021) 125–128.
- [40] J. Zhao, M. Easton, M. Qian, M. Leary, M. Brandt, Effect of building direction on porosity and fatigue life of selective laser melted AlSi12Mg alloy, Mater. Sci. Eng. A 729 (2018) 76– 85
- [41] H. Qu, J. Li, F. Zhang, J. Bai, Anisotropic cellular structure and texture microstructure of 316L stainless steel fabricated by selective laser melting via rotation scanning strategy, Mater. Des. 215 (2022) 110454.
- [42] H. Yeung, B.M. Lane, M. Donmez, J.C. Fox, J. Neira, Implementation of advanced laser control strategies for powder bed fusion systems, Procedia Manuf. 26 (2018) 871–879.
- [43] M.E. Cox, E.J. Schwalbach, B.J. Blaiszik, M.A. Groeber, AFRL additive manufacturing modeling challenge series: overview, Integr. Mater. Manuf. Innov. 10 (2) (2021) 125–128.
- [44] Z. Gan, Y. Lian, S.E. Lin, K.K. Jones, W.K. Liu, G.J. Wagner, Benchmark study of thermal behavior, surface topography, and dendritic microstructure in selective laser melting of Inconel 625, Integr. Mater. Manuf. Innov. 8 (2) (2019) 178–193.
- [45] R.A. Davis, K.-S. Lii, D.N. Politis, Remarks on some nonparametric estimates of a density function, in: R.A. Davis, K.-S. Lii, D.N. Politis (Eds.), Selected Works of Murray Rosenblatt, Springer New York, 2011, pp. 95–100.
- [46] S. Kullback, R.A. Leibler, On information and sufficiency, Ann. Math. Stat. 22 (1) (1951)
- [47] W.K. Hastings, Monte Carlo sampling methods using Markov chains and their applications, Biometrika 57 (1970) 97–109.
- [48] D. Whitley, A genetic algorithm tutorial, Statist. Comput. 4 (2) (1994) 65–85. [49] Y. Lu, N. Blal, A. Gravouil, Adaptive sparse grid based HOPGD: Toward a nonintrusive strategy for constructing space-time welding computational vademecum, Internat. J. Numer. Methods Engrg. 114 (13) (2018) 1438–1461.
- [50] Y. Lu, N. Blal, A. Gravouil, Datadriven HOPGD based computational vademecum for welding parameter identification, Comput. Mech. 64 (1) (2019) 47–62.
- [51] Y. Lu, N. Blal, A. Gravouil, Multi-parametric space-time computational vademecum for parametric studies: Application to real time welding simulations, Finite Elem. Anal. Des. 139 (2018) 62–72.
- [52] Y. Lu, N. Blal, A. Gravouil, Space–time POD based computational vademecums for parametric studies: application to thermo-mechanical problems, Adv. Model. Simul. Eng. Sci. 5 (1) (2018) 1–27.
- [53] Z. Gan, K.K. Jones, Y. Lu, W.K. Liu, Benchmark study of melted track geometries in laser powder bed fusion of inconel 625, Integr. Mater. Manuf. Innov. 10 (2) (2021) 177–195.
- [54] S. Saha, O.L. Kafka, Y. Lu, C. Yu, W.K. Liu, Microscale structure to property prediction for additively manufactured IN625 through advanced material model parameter identification, Integr. Mater. Manuf. Innov. 10 (2) (2021) 142–156.
- [55] A.A. Amin, Y. Li, Y. Lu, X. Xie, Z. Gan, S. Mojumder, G.J. Wagner, W.K. Liu, Physics guided heat source for quantitative prediction of IN718 laser additive manufacturing processes, npj Comput. Mater. 10 (1) (2024) 37.

- [56] J. Ye, S.A. Khairallah, A.M. Rubenchik, M.F. Crumb, G. Guss, J. Belak, M.J. Matthews, Energy coupling mechanisms and scaling behavior associated with laser powder bed fusion additive manufacturing. Adv. Eng. Mater. 21 (7) (2019).
- [57] R. Fabbro, M. Dal, P. Peyre, F. Coste, M. Schneider, V. Gunenthiram, Analysis and possible estimation of keyhole depths evolution, using laser operating parameters and material properties, J. Laser Appl. 30 (3) (2018) 032410.
- [58] H. Guo, P. Feissel, F. Druesne, S. Bouzebda, N. Limnios, A. Patigniez, S. Bouyaux, An identification strategy for stochastic fatigue models of welding joints from structural experiments, Eng. Struct. 270 (2022) 114860.
- [59] X. Xie, J. Bennett, S. Saha, Y. Lu, J. Cao, W.K. Liu, Z. Gan, Mechanistic data-driven prediction of as-built mechanical properties in metal additive manufacturing, npj Comput. Mater. 7 (1) (2021) 86.
- [60] D.P. Kingma, J. Ba, Adam: A method for stochastic optimization, 2014, arXiv preprint arXiv:1412.6980.
- [61] E.P. DeGarmo, J.T. Black, R.A. Kohser, B.E. Klamecki, Materials and process in manufacturing, 1997.
- [62] U.S. Bertoli, A.J. Wolfer, M.J. Matthews, J.-P.R. Delplanque, J.M. Schoenung, On the limitations of volumetric energy density as a design parameter for selective laser melting, Mater. Des. 113 (2017) 331–340.
- [63] I. Koutiri, E. Pessard, P. Peyre, O. Amlou, T. De Terris, Influence of SLM process parameters on the surface finish, porosity rate and fatigue behavior of as-built Inconel 625 parts, J. Mater. Process. Technol. 255 (2018) 536–546.
- [64] B. Lane, H. Yeung, Process monitoring dataset from the additive manufacturing metrology testbed (ammt): Overhang part x4, J. Res. Natl. Inst. Stand. Technol. 125 (2020) 1–18.
- [65] M. Praniewicz, B. Lane, F. Kim, C. Saldana, X-ray computed tomography data of additive manufacturing metrology testbed (AMMT) parts:" overhang part X4", J. Res. Natl. Inst. Stand. Technol. 125 (2020) 1–9.
- [66] Y. Lu, K.K. Jones, Z. Gan, W.K. Liu, Adaptive hyper reduction for additive manufacturing thermal fluid analysis, Comput. Methods Appl. Mech. Engrg. 372 (2020) 113312.
- [67] S. Sharma, S.S. Joshi, M.V. Pantawane, M. Radhakrishnan, S. Mazumder, N.B. Dahotre, Multiphysics multi-scale computational framework for linking process– structure– property relationships in metal additive manufacturing: a critical review, Int. Mater. Rev. (2023) 1–67.
- [68] Capriccioli, P. Frosi, FE procedure for welding processes simulation, 2009.
- [69] R.E. Pawel, R.K. Williams, Survey of physical property data for several alloys. [nitronic 33; copper C10400; copper C17510], vol. 17, no. 6, 1985.
- [70] J.J. Valencia, P.N. Quested, Thermophysical properties, 2013.
- [71] H. Yeung, B. Lane, A residual heat compensation based scan strategy for powder bed fusion additive manufacturing, Manufact. Lett. 25 (2020) 56–59.
- [72] M.C. Kennedy, A. O'Hagan, Bayesian calibration of computer models, J. R. Stat. Soc. Ser. B Stat. Methodol. 63 (3) (2001) 425–464.
- [73] L. Devroye, L. Györfi, G. Lugosi, A Probabilistic Theory of Pattern Recognition, vol. 31, Springer Science & Business Media, 2013.